Chapter 6

Porous Nanocarbons: Molecular Filtration and Electronics

Boyang Wang, Artem Baskin and Petr Král

Additional information is available at the end of the chapter

http://dx.doi.org/10.5772/56247

1. Introduction

Graphene is an atomically thick monolayer formed by hexagonally arranged carbon atoms with sp^2 planar covalent bonds [1]. It has unique mechanical [2], electronic [3], optical [4], and transport properties [5], leading to many potential applications [6]. Its low-energy electron excitations are 2D massless chiral Dirac fermions [3], moving 300 times slower than light [7]. These fermions have nearly ballistic transport and high mobility at room temperature [3, 5, 7–9]. In magnetic fields, their motion is associated with several quantum Hall effects, observable at room temperature [10, 11]. Many methods have been proposed to fabricate large-area semiconducting graphene materials, such as chemical [12–14], sonochemical [15], and lithographic [16, 17] methods. Graphene is a great candidate for electronic applications [6], especially upon further functionalization [18–20]. Graphene was modified by wrapping [21–24], oxidation [25–27], etching [12, 28, 29], covalent [20, 30–34], noncovalent [20, 35], and biological [36] functionalization.

Despite the fact that graphene has excellent transport characteristics, its applicability in semiconductor industry is limited, since it lacks a significant band gap $\gg kT$ [3]. Therefore, graphene conductance can not be easily modified by doping and electric fields, as in silicon [37]. However, a band gap can be opened in geometrically restricted graphene [5, 38–42]. The simplest restrictions originate in edges [43], giving graphene unique structural [44–46], electronic [39, 41] and chemical properties [47]. Graphene edges have been modified [48, 49] by selective chemical bonding [50] and etching [29, 51]. They have been controlled by electrochemical [52] and optical [53] means, and characterized spectroscopically [54–56]. When graphene is restricted by two parallel edges, a graphene nanoribbon (GNR) is formed with armchair (AGNR) or zig-zag edges (ZGNR). Metallic or semiconducting GNRs can be obtained by cutting graphene [57], carbon nanotubes or by purely organic means [58]. While tight-binding calculations showed that AGNRs appear to be metallic at certain widths [59],

DFT calculations predicted that all AGNRs are semiconducting, with a band gap roughly inversely proportional to the GNR width [59–62], but all ZGNRs are semimetallic.

Alternatively, graphene can be restricted by perforation with nanopores, in analogy to a two-dimensional Swiss cheese [63, 64]. Graphene nanopores can be functionalized to create materials with rich applications in physics [65], chemistry [66, 67], biology [68] and various technologies [69, 70], such as molecular separation [63, 71–75] and electronics [6, 62, 76]. Chemical functionalization of graphene nanopores can improve their separation ability [63, 77–83], and detection [74, 84]. For example, oxidation of packed multilayered graphene sheets could allow selective ultrafast water flows through these layers, and prevent the passage of helium, nitrogen, argon, and hydrogen [80]. Nitrogen substitutions of carbon atoms in the pore rims are important for a quick separation of ^{3}He and ^{4}He nuclei [77]. Diamond-like carbon nanosheets with nanopores can selectively filtrate organic solvents [81], such as ethanol and azobenzene.

2. Preparation of porous nanocarbons

The porous graphene can be prepared by top down and bottom up approaches. In the top down approach, nanopores can be drilled in graphene by electron beams [73, 85–87] or by oxidative [64, 75, 88] and steam [89] etching. In Fig. 1 (left), an electron-beam drilled nanopore in graphene is shown [73]. This pore has been used to detect the passage of ionic solutions and DNA molecules [73, 86, 87]. Graphene nanopores prepared by oxygen plasma etching [64] have homogeneous distribution of sizes, which leads to opening of an effective energy gap of 100 meV in the graphene material. Steam etching of graphene by water vapor in a seal vessel at 200 K temperature is a rather slow process [89], but with a better control of the porosity by the etching time.

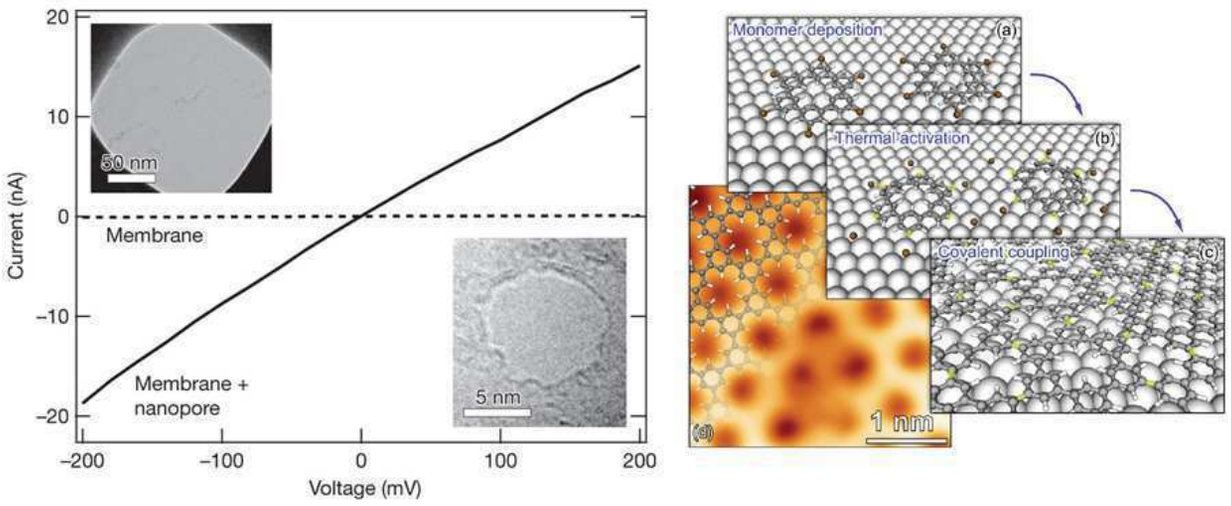

Figure 1. (left) Experimentally prepared graphene nanopore by electron beam drilling. From Ref. [73]. (right) Synthetic growth of porous graphene from organic molecules covalently bound on the surfaces of metals. From Ref. [90].

Precise graphene nanopores could also be prepared by bottom up approaches, where porous graphene can be grown from conjugated aromatic molecules covalently interconnected on the surfaces of other materials (metals). In Fig. 1 (right), we show graphene nanopores with precisely functionalized rims experimentally prepared in this manner [90]. This procedure

uses surface-assisted coupling of molecular precursors into linear polyphenylenes and their subsequent cyclodehydrogenation. The porous graphene was synthesized by depositing hexaiodo-substituted macrocycle cyclohexa-m-phenylene (CHP) on Ag (111) surface, and annealing to temperatures above 570 K initiates the polymerization reaction. Six-fold aryl-aryl coupling of the CHP monomers resulted in a 2D polyphenylene network. This contained periodic nanopores in a hexagonal pattern in the polymerized graphene layer, also with atomic precision. Another bottom up approach used the self-assembly of close-packed polystyrene nanospheres to synthesize semiconducting porous graphene networks [62]. Highly ordered networks of carbon atoms based on non-covalent interactions, such as hydrogen bonding, metal coordination, or aromatic interactions have also been grown on various single crystalline substrates [58, 90, 91].

Although both the bottom up and top down approaches create porous graphene with a band gap, the amount of imperfections is significantly smaller in the first approach. This is of importance for electronic and optical applications [6]. Field effect transistors made of porous graphene fabricated in a top down way demonstrate a high hole mobility at room temperature [64]. In a functionalized and modified graphene, spectroscopic methods are used to characterize the electronic states [51, 92] and chemical structures before [92–98] and after [99–101] modifications. These methods include Raman [99, 102–105], resonance-Raman [51], surface-enhanced Raman [106], infrared [95, 107–109], plasmon [110], nuclear magneto-resonance [111], scanning tunneling [95, 112], photoemission [113] and Auger electron spectroscopies [114].

3. Ionic and molecular separation by graphene nanopores

Biological ionic channels play a key role in many cellular transport phenomena [115]. The large selectivity of these proteins is realized by precisely arranged arrays of charged amino acids that can efficiently recognize and guide the fast passing ions [116]. Much simpler non-biological ionic and molecular channels are made from zeolites [117], carbon [118], silica [119] and other materials [120, 121]. For many industrial applications, these channels are often not selective and transparent enough. Therefore, ion and molecular channels with novel structures and recognition principles need to be designed.

Molecular dynamics studies have predicted [122] and experiments have demonstrated fast transport of gases [123, 124] and liquids [125–128] through carbon nanotube (CNT) membranes. Hydrated ions could also pass through CNTs of large enough diameters [129]. Recently, graphene [1] and boron-nitride [130] monolayers have been prepared and intensively studied [131–133] for their many potential applications. The first is a semimetal that can screen free charges (screening length of 4 Å [134]), while the second is a semiconductor with a large band gap that screens charges very little.

3.1. Ionic and atomic separation by graphene nanopores

Note that graphene layer is impermeable to even small atoms, such as helium [135]. However, recently, functionalized nanopores in graphene monolayers have been theoretically designed and have shown that they could serve as ionic sieves of high selectivity and transparency [63], in analogy to natural functional proteins [136–138].

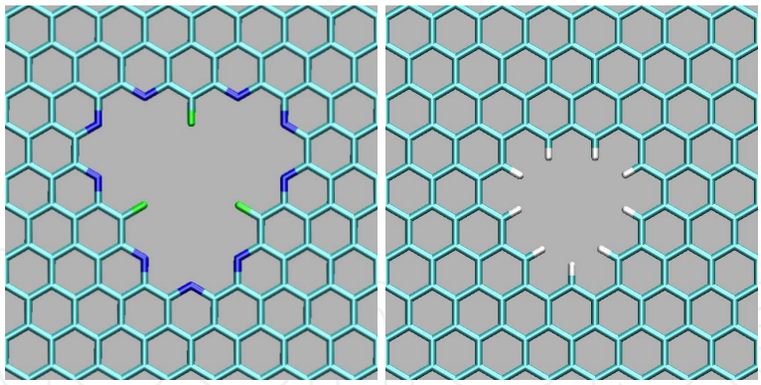

Figure 2. Functionalized graphene nanopores. (Left) The F-N-terminated nanopore. (Right) The H-terminated nanopore. From Ref. [63].

In Fig. 2, we display the studied chemically modified graphene nanopores. The F-N-pore (left) is terminated by negatively charged nitrogens and fluorines, favoring the passage of cations. The H-pore (right) is terminated by positively charged hydrogens, favoring the passage of anions. These nanopores could be formed in the graphene monolayers by ion etching [139], and their chemical modifications could be realized by local oxidation, similarly as on graphene edges [140, 141].

We modeled the passage of hydrated ions from the first and seventh periods through these tiny nanopores. Our molecular dynamics (MD) simulations [142–144] were performed with the NAMD package [145], based on the CHARMM27 force field [146]. The model graphene sheets (sizes of 23x23 Å) have chemically modified nanopores in their center. The atomic charges of these sheets are obtained ab initio with B3LYP density functional [147], using the Gaussian03 package [148]. These calculations show that when the ion passes through the graphene nanopore, the semimetallic sheet becomes highly polarized.

Therefore, a screening charge of the same size but opposite sign to that of the ion goes to the pore rim and an opposite charge remains spread on the rest of the sheet. In the presence of water the screening charge should be more delocalized at the pore entrance, due to water polarization. In the MD simulations, we model these effects by homogeneously spreading the screening charge for the studied ion on the first atomic layer of the pore and the atomic ligands attached to it. The screening charge is kept there during the whole simulations, since its presence is little affecting the dynamics when the ion is far away from the pore. The opposite polarization charge on the sheet is neglected, for simplicity, so the combined system of the ion and the sheet is kept neutral.

In the simulations, the sheet is placed in a periodic unit cell with 10 Å of water (320 waters in total) on each side. One ion is placed in the cell and driven by an electric field E applied in the direction perpendicular to the graphene sheet. Each simulation run typically lasts 100-500 ns. It turns out that the F-N-pore is only passed by the Li^+, Na^+ and K^+ ions, while the H-pore is only passed by the Cl^- and Br^- ions. This selectivity of the nanopores, even in the presence of large driving field of E = 0.1 V/nm, is caused by the Coulombic coupling between the ion and the functionalized nanopore rim. At this field, the passage rates of Li^+, Na^+ and K^+ have the ratio of 9:14:33, while those of F^-, Cl^- and Br^- have the ratio of 0:17:33. Therefore, the nanopores are also highly selective to the sizes of the ions. The Li^+ and F^- ions have the lowest passage rates, because of their small radii and large coupling to

http://dx.doi.org/10.5772/56247

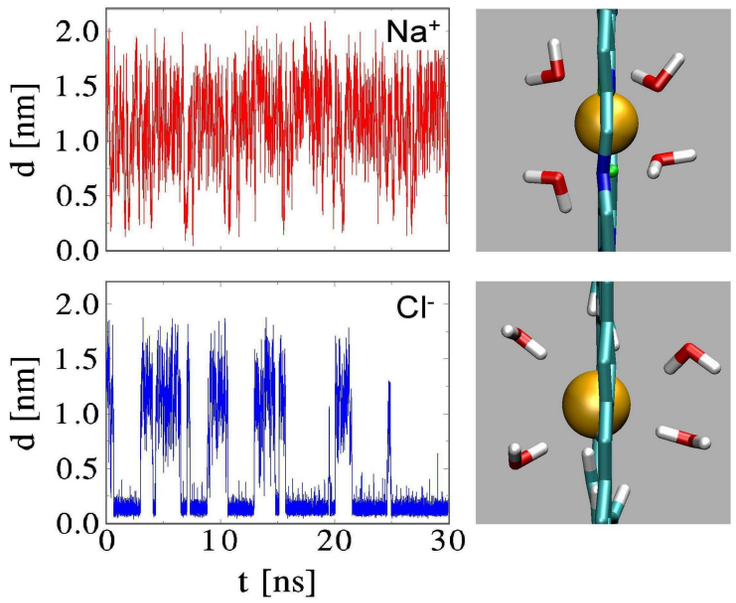

Figure 3. (left) The time-dependent distance d between the Na^+ and Cl^- ions and the centers of the F-N-pore and H-pore, respectively, at the field of E = 6.25 mV/nm. The ion passages through the two nanopores have very different dynamics. (right) The passing ions are surrounded by two water half-shells, but only Cl^- has relatively stable binding to the pore. From Ref. [63].

the water molecules in their hydration shells. On the contrary, K^+ and Br^- have large radii, so it is relatively easy to break their hydration shells in the pores.

In Fig. 3 (right insets), we also show the configurations of the selected Na^+ and Cl^- ions passing through the two nanopores. The polar and charged rims replace some of the water molecules from the first hydration shell of the ions passing through the nanopores. Due to the atomic thickness of the graphene layer, the passing ion is surrounded by two separated first hydration half-shells at its both sides. The close contact between the pore rim and the ion leads to the high selectivity of the ion passage.

Fig. 3 (left insets) displays the time-dependent distance d between the ions and their pore centers, obtained at the low field of $E = 6.25$ mV/nm. The character of the obtained fluctuations reveals that the ion passages through the two nanopores have very different dynamics [149]. The Na^+ ion passes the F-N-pore rather fast, without binding with it. It rarely gets closer than 5 Å to the pore center and stays most of the time in the water region ($d > 10$ Å). The ion does not pass through the pore center, but rather through one of the three smaller holes in the nanopore with the C_3 symmetry. This asymmetric hole can not easily break the hydration shell of the Na^+ ion. The K^+ ion binds weaker to its hydration shell and it starts to bind to the pore.

The Cl^- ion has more stable binding to the symmetric H-pore, where it already stays for about 70% of the time. The electric field decreases the ion-pore binding, which is reflected in shorter time periods spent by the ion in the pore. At the field of $E = 0.1$ V/nm, the Cl^- ion already stays in total only 30% of the time inside the pore. The unidirectional ion flow in the presence of electric field is reflected in the slight left-right asymmetry in the number of entrances of the ion in the nanopore and exits out of it.

Figure 4 shows the results of the ion flow through the system at different fields E. We display the field dependence of the average number of Na^+ and Cl^- ion passages, r_{Na} and

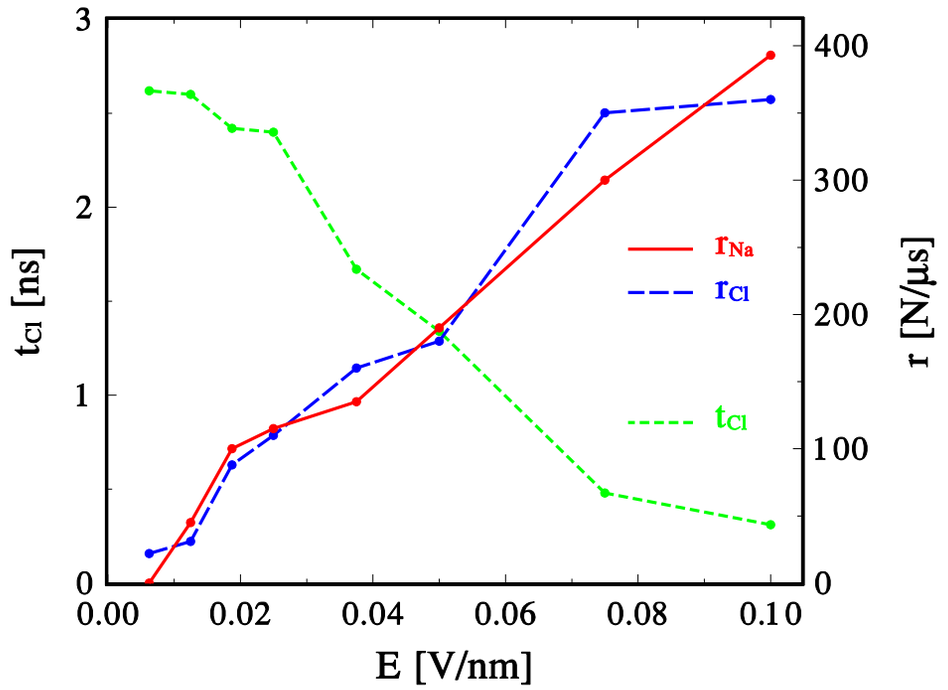

Figure 4. (right axis) Dependence of the r_{Na} and r_{Cl} flow rates of the hydrated Na^+ and Cl^- ions through the F-N-pore and H-pore, respectively, on the applied electric field E. (left axis) The average time t_{Cl} spent by the Cl^- ion inside the H-pore. From Ref. [63].

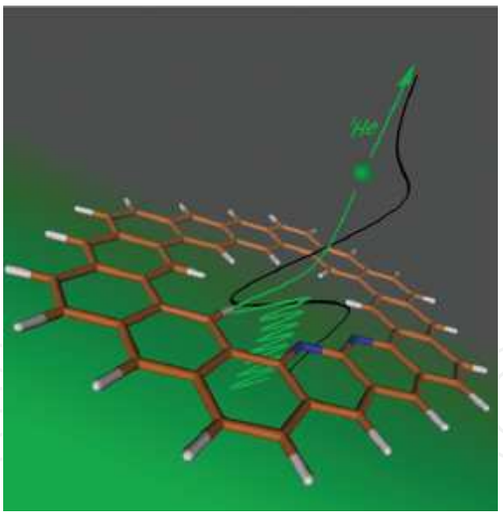

Figure 5. A graphene nanopore functionalized by nitrogen atoms, used in the separation of ^{3}He and ^{4}He isotopes. From Ref. [77].

r_{Cl}, through the F-N-pore and the H-pore, respectively. Both rates monotonously grow with the field, showing the accelerated passage of the ions through the pore and the surrounding water layers. We also show the field-dependence of the average residence time t_{Cl} of the Cl^- ion in the H-pore, defined as the time during which the ion stays within the 5 Å distance from the pore center. We can see that t_{Cl} decreases monotonously with the field that helps the ion to overcome the Coulombic binding to the nanopore.

http://dx.doi.org/10.5772/56247

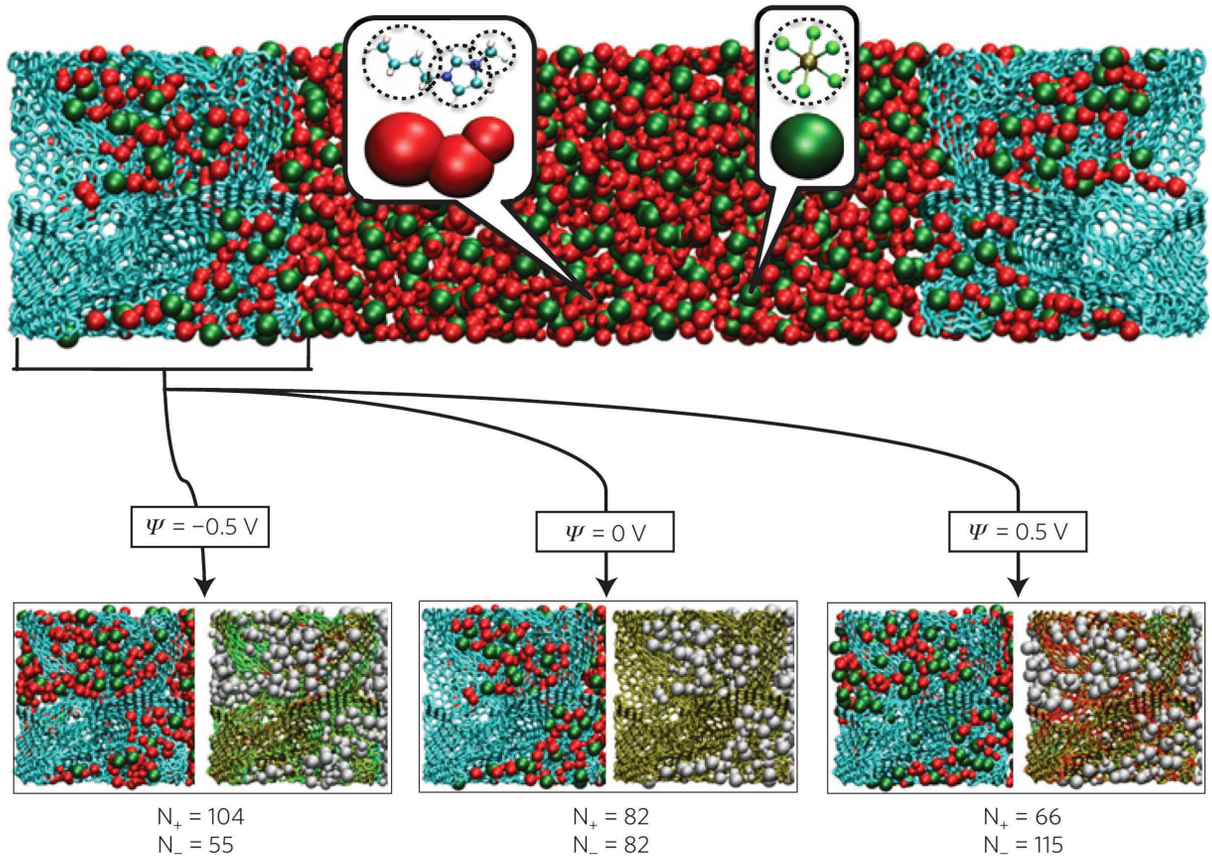

Figure 6. The EDLC simulation cell. Upper panel: the simulation cell consists of a BMI-PF_6 ionic liquid electrolyte surrounded by two porous electrodes (CDC-1200) held at constant electrical potentials (blue: C atoms, red: the three sites of BMIC and green: PF_6 ions; a coarse-grained model is used to describe these ions). Lower panel: structure of the electrode for various voltages. For each value, the same snapshot is shown twice: The ionic distribution is shown on the left. The degree of charging of the electrode atoms is shown on the right, where the carbon atoms are coloured according to the charge q they carry (green: $q < 0$, red: $q > 0$ and yellow: $q = 0$). From Ref. [151].

The above results have shown that chemically functionalized nanopores in graphene monolayers can have a high selectivity for the passage of hydrated ions. These ionic and molecular nanopores could be optimally designed [150] by choosing the type of monolayer material, the pore sizes and the structure/number of ligands attached to their rims. These ultrasmall nanopores could be applied in molecular separation, desalination and battery technologies.

Selective atom passage through graphene nanopores was also studied by first principle techniques [77]. In Fig. 5, we show the configuration of one of the studied systems with a chemical structure possibly matching the separated ^{3}He and ^{4}He isotopes. The tunneling rates of the isotopes through the different nanopores were calculated. The barriers for ^{3}He to pass through the three nanopores were found to be very different one from another. The hydrogen, half-nitrogen (one side), and full-nitogen (both sides) terminated nanopores had the barriers, $\approx$ 0.078 eV, $\approx$ 0.025 eV, and $\approx$ 0.0076 eV, respectivelly. To achieve a high flux through the nanopore, while keeping a large difference in the transimission probabilities of ^{3}He and ^{4}He isotopes through the nanopore, the one-sided nitrogen doped pore (the second pore) was chosen, as shown in Fig. 5. The transmission ratio between ^{3}He and ^{4}He was 2 at 20 K, and raised with decreasing temperature to 19 at 10 K.

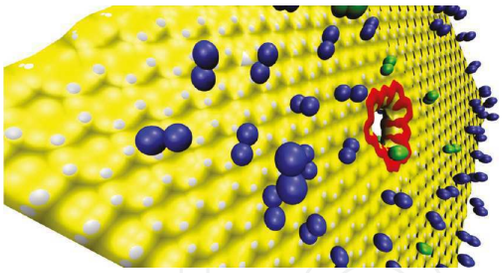

Figure 7. The graphene nanopore used in separations of hydrogen and nitrogen gases. The graphene sheet is represented by a yellow plane with white points referring to carbon atoms, and the pore shape is colored by red; hydrogen and nitrogen molecules are colored by green and blue, respectively. From Ref. [152].

Porous graphene could also be used as a unique material for electrodes in supercapacitors and batteries, as shown in recent simulations with polarizable force fields [151]. In Fig. 6 the studied system is shown. Upon charging the porous nanocarbon electrodes, ionic liquid electrolytes could enter into them through the nanopores. The anode retains more anions than cations, and the cathode retains more cations than anions. The supercapacitor formed could store charges with a very high efficiency.

3.2. Molecular separation by graphene nanopores

In the separation of neutral molecules by graphene nanopores, van der Waals interactions are crucial, since size exclusion is the main separation mechanism. Recently, for example, the separation of nitrogen and hydrogen gases in graphene nanopores have been examined by MD simulations [152], as shown in Fig. 7. In the minimal graphene nanopore size studied here, hydrogen molecules could pass through the pore and nitrogen molecules were totally excluded. When the graphene pore size became larger, N_2 passed through the nanopore much faster than H_2 due to a different mechanism. It was found that N_2 was largely adsorbed on the graphene surface, due to strong van der Waals attraction, and it diffused on it, before reaching the pore. On the other hand, H_2 was much less adsorbed on the graphene, and it had to diffuse in the 3D space before reaching the nanopore.

It was also shown by MD simulations that graphene nanopore could enhance the separation of carbon dioxide from nitrogen molecules [153]. Separation of hydrogen molecules from methane molecules based on the size exclusion mechanism was also investigated by ab initio methods [71]. The potential energy surfaces of a hydrogen and methane molecules passing through a chemically modified graphene nanopore were obtained by density functional methods. A dramatic difference between these two potential energy surfaces was found, which caused a highly efficient separation of hydrogen molecules from methane molecules. It was also shown that methane could be separated from air by graphene nanopores [154], which could serve as atmospheric nanofilters [155].

The flow of water through graphene nanopores was also simulated [72] in a configuration shown in Fig. 8. The passage of a single water molecule through such a small graphene nanopore necessitates it to break most of its hydrogen bonds, which significantly slows down the water flux through the nanopore (two water molecules that are separated by the graphene nanopore have one hydrogen bond in common). As the pore size increase so does the flux. Graphene nanopore of a diameter $d > 0.8$ nm were proven to have higher water flux than a carbon nanotube of the same diameter. Therefore, porous graphene could have significant applications in desalination [156].

http://dx.doi.org/10.5772/56247

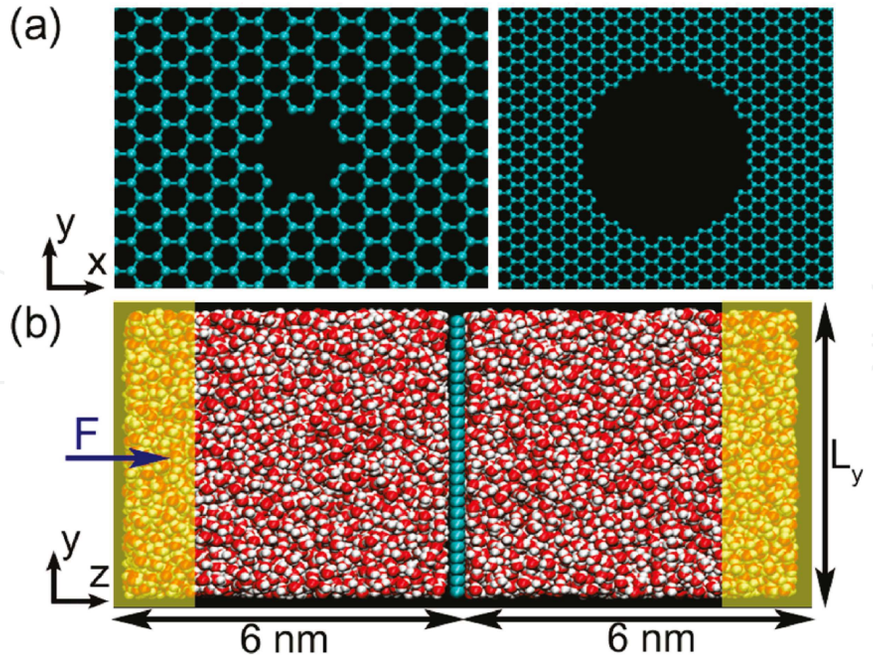

Figure 8. (a) Graphene membrane with a nanopore of diameter $d_{avg} = 0.75$ nm (left) and $d_{avg} = 2.75$ nm (right). (b) Simulation setup. Cyan color represents carbon atom, red color and white color represent the oxygen and hydrogen atoms of a water molecule, respectively. Two water reservoirs are attached to each side of the porous graphene membrane. $L_y = L_x = 4$ nm when the pore diameter is 0.75 nm, and $L_y = L_x = 6$ nm when the pore diameter is 2.75 nm. In the shaded region ($z = 1$ nm), external forces are applied on water molecules to create a pressure drop across the membrane. From Ref. [72].

It was shown that graphene with nanopores could be a good candidate for water desalination [156, 157]. Traditional water desalination industry applied polymeric reverse osmosis membranes, which had high salt rejection, but with a very low water flux rate. Graphene nanopores could selectively reject salt [157], and with a water flux several orders of magnitude higher than polymeric reverse osmosis membranes. The salt rejection mechanism is based on size exclusion [157], since salt ions have hydration shells that are much bigger than single water molecules. The maximal diameter of the hydrogen-terminated nanopore that could reject salt is 5.5 Å. The salt rejection rate decreases at higher pressures, since the ion hydration shells break. Since, large areas of graphene can be grown on copper foils [158], it is likely that graphene membrane can have industrial applications for water desalination in the future.

Recently, other graphene-based filtration membranes were studied as well. For example, small pieces of graphene oxide (GO) were packed to form multilayered membranes [80], shown in Fig. 9 (a-b). In each layer of the membrane, the GO pieces were disconnected, with empty space between the pieces, as shown in Fig. 9 (c). When water was adsorbed on the membrane, it found empty spaces in each GO layer and protruded toward the next layer. In this way, water was able to penetrate through the whole membrane. However, such water permeable GO membranes prevents the leakage of He gas, as shown in Fig. 9 (d).

Graphene nanopores could also be used for DNA sequencing [73, 86, 87, 159]. Previous sequencing nanopores were relatively thick and retained multiple DNA base pairs inside the nanopore during the sequencing process, so the detection of these bases were not efficient. On the contrary, graphene nanopores can provide detection within an atomically thick

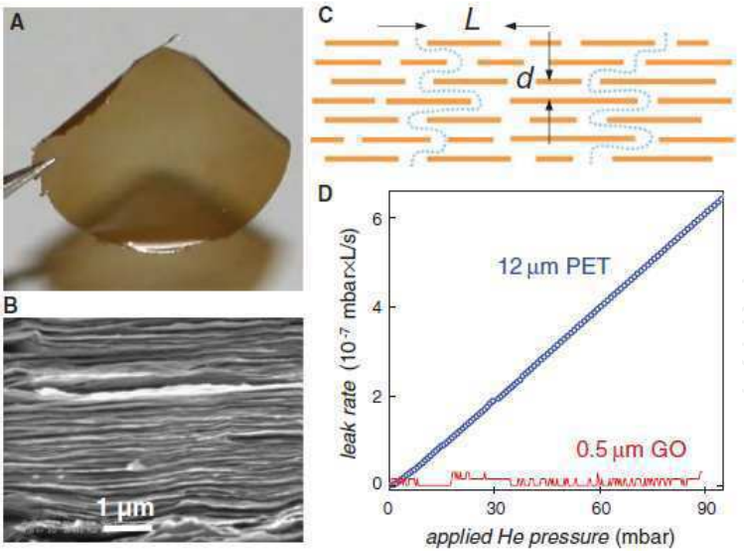

Figure 9. He-leak through GO membranes. (A) Photo of a 1-mm-thick GO film peeled off of a Cu foil. (B) Electron micrograph of the films cross section. (C) Schematic view for possible permeation through the laminates. Typical L/d is 1000. (D) Examples of He-leak measurements for a freestanding submicrometer-thick GO membrane and a reference PET film (normalized per square centimeter). From Ref. [80].

monolayer. The detection of DNA basis might be possible to deduce from the fluctuations of ionic currents passing simultaneously with the DNA through the graphene pores.

In the experiments [73], double stranded DNA molecules and solvated ions were electrophoretically passed through a 5 nm graphene nanopore, shown in Fig. 1 (left). Ions could pass smoothly through the nanopore, and their electric current is proportional to the applied voltage. However, other molecules present in the nanopore reduce the ion current. When a DNA molecule passes through the nanopore, it causes electric current blocade, and reduces the current for a certain time, which can reflected the size and conformation of the passing DNA. If the DNA molecule is folded, then the blocade duration is short (e.g. on the order of 10 microseconds). When the DNA is unfolded, it passes the nanopore as a linear chain, and the current blocade lasts for a longer time (e.g. 200 microseconds). In this way, details about the DNA molecule and its passage through the graphene nanopore could be detected.

The passage of DNA through a graphene nanopore was also investigated by MD simulations in the presence of electric fields [74, 160]. To make sure that DNA translocation through the nanopore completes within a time scale that is accessible for molecular dynamics, a bias voltage of $\phi = 2.1$ V was applied to the system. It turned out that additional charges at the nanopore also influenced the field-driven DNA passage through the nanopore. A positively charged nanopore allowed faster transport of DNA through the nanopore than negatively charged ones, since DNA alone is negatively charged. Figure 10 shows a trajectory of DNA conformations during the translocation through the nanopore within 15 ns in the electric field. The partially folded DNA had various conformations while passing through pore, and the electric current fluctuated with these conformations. When part of the DNA was inside the nanopore, the current had different peaks signifying the translocation events. It was shown that poly(A-T)20 and poly(G-C)20 duplexes passing through the nanopore produce different ionic current profiles. This means that A-T and G-C base pairs could be distinguished. Molecular and atomic species passing through graphene nanopores

http://dx.doi.org/10.5772/56247

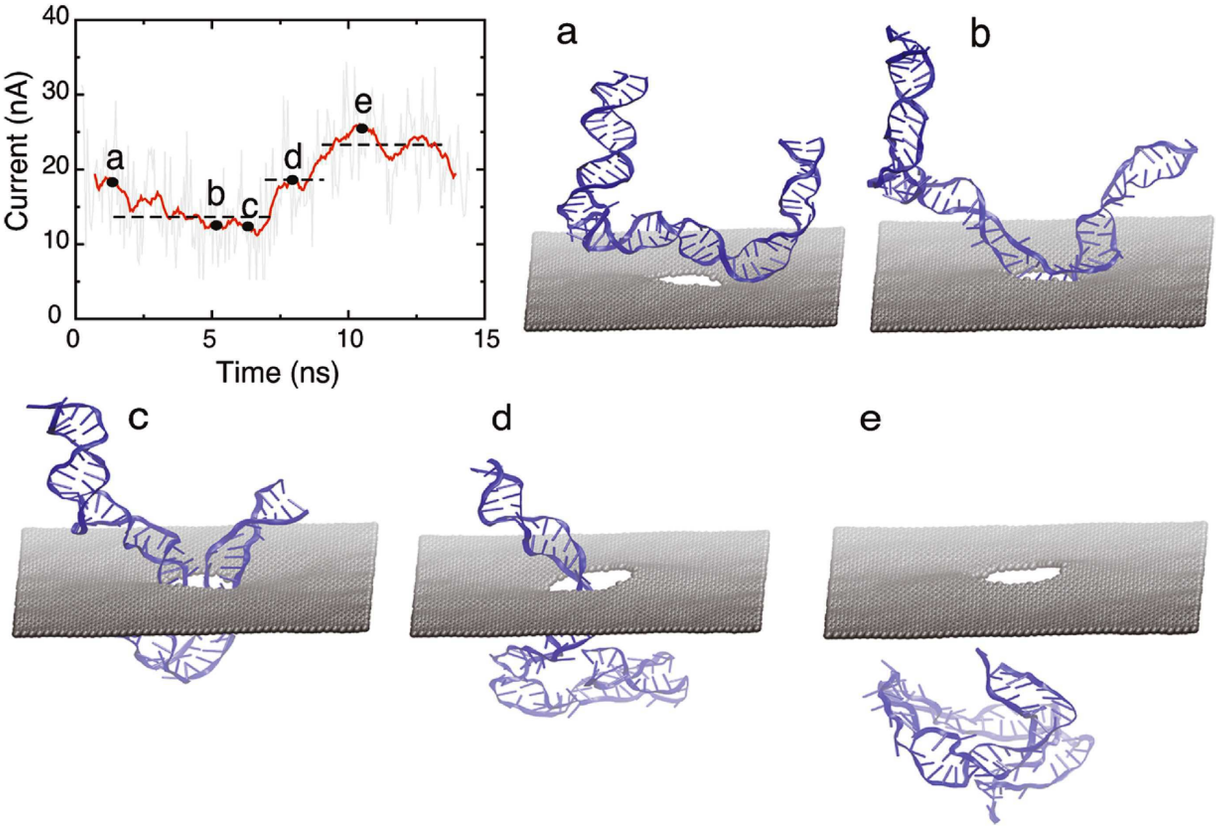

Figure 10. Translocation of partially folded DNA. The three dotted lines correspond to plateaus in ionic current signature. Snapshots of DNA conformation during translocation is shown in (a-e). (a) Initial conformation of DNA; (b) DNA captured by pore mouth; (c) both chains of folded DNA in the pore; (d) one chain leaves pore; (e) DNA exits the pore completely. The diameter of the pore is 3 nm and the bias voltage was 2.1 V. From Ref. [74].

could in principle be detected electronically from the change of the electronic structure of porous nanocarbons in the presence of passing molecules [71]. For example, the electron transmissivity of porous nanocarbons may significantly vary when the particular molecule passes through the pore [161–163].

4. Electronic Structure/Transport in Porous Nanocarbons

Given the discussed possibilities of molecular separation and detection in graphene nanopores, it is important to understand the electronic structure of porous graphene in vacuum and in the presence of molecular fields. Therefore, we review the electronic properties of *porous nanocarbons* (PNCs), as shown in Fig 11. In general, PNCs are derived from graphene, carbon nanotubes (CNT), and nanoribbons (GNR) by introduction of functionalized pores. These nanopores allow tuning of their electronic structures, which can be useful in a wide range of electronics applications [164–169].

4.1. Electronic structures of porous nanocarbons

The main effects that the pores cause in pristine nanocarbons are: 1) the energy band gap opening; 2) the emergence of midgap energy states; 3) flat and quasi-flat bands at zero and low non-zero energies. Although, partial results for the electronic structures of porous

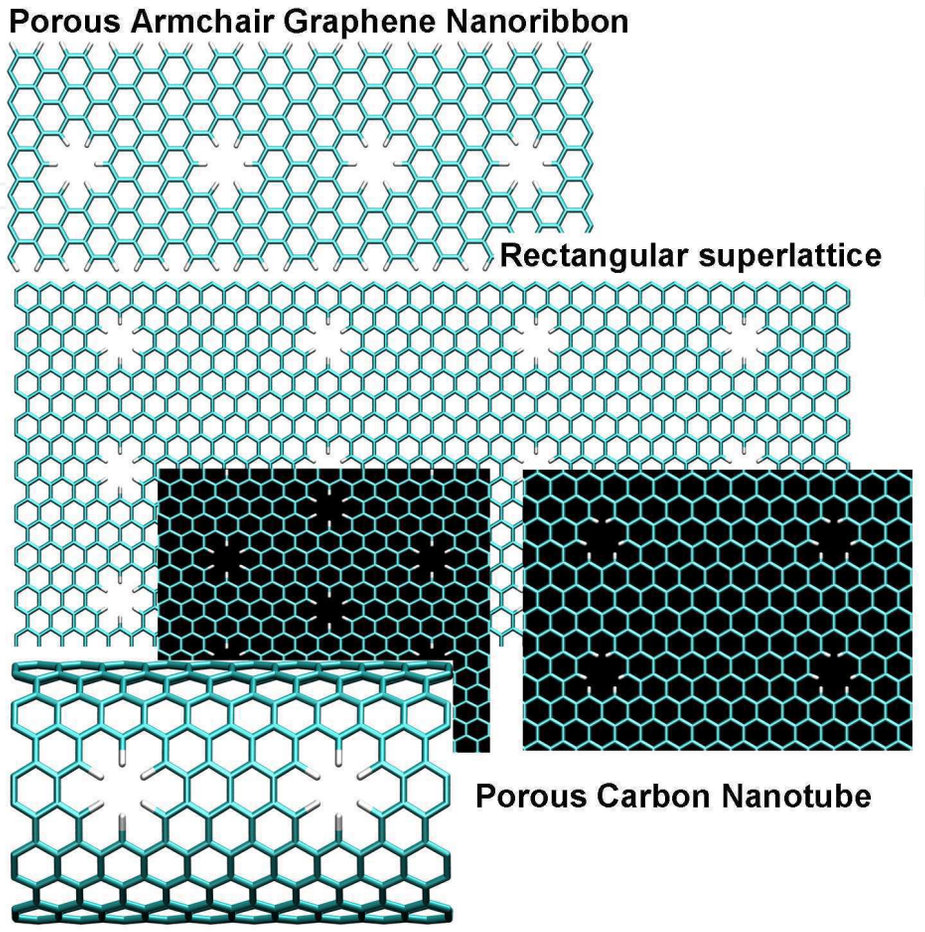

Figure 11. Examples of PNCs.

graphene [167–169] and other PNCs have been obtained [5, 59, 170–173], general principles that would unify their electronic structures are missing.

Graphene and its derivatives were studied theoretically by a variety of methods, such various DFT and tight-binding (TB) approaches, using semiempirical parametrization of electron-electron interactions in model Hamiltonians [168, 169]. The pseudo-relativistic behavior of electrons close to the Fermi level in graphene can be modeled by a Dirac equation (DE) [167]. Semiempirical approaches were also used, such as the Hückel molecular orbital method [170, 173], crystal orbital methods [174], or mean-field resonating-valence-bond theories designed to treat unpaired π-electrons in benzenoid carbon species [175]. The principal problem for any theoretical approach dealing with PNCs is to determine the correlation between geometrical structure of PNCs and their electronic structures. Therefore, we will focus on this correlation and describe it separately for different PNCs systems.

Porous graphene nanoribbons (PGNRs)

Graphene and its nanoribbons can be directly grown on material surfaces. Therefore, graphene-based materials could have direct applications in nanoelectronics. In contrast to pristine 2D graphene sheets and CNTs, GNRs have (armchair, zigzag, or mixed) edges.

http://dx.doi.org/10.5772/56247

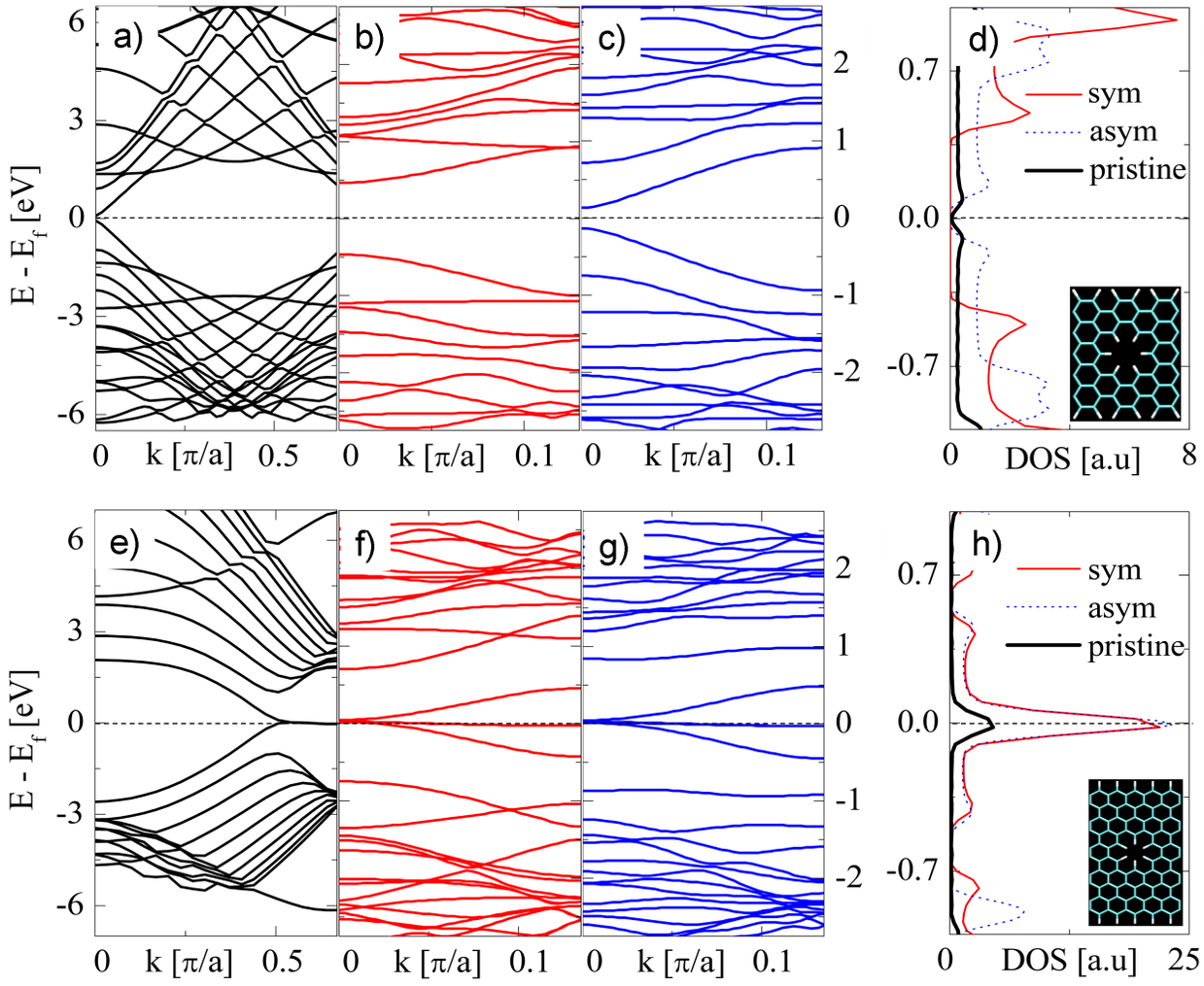

Figure 12. Band structure of: a) pristine 11-AGNR, b) 11-AGNR with centered SP, c) 11-AGNR with shifted SP, e) pristine 10-ZGNR, f) 10-ZGNR with centered SP, g) 10-ZGNR with shifted SP. The energy scales for (b, c, f, g) cases are the same. Density of states: d) centered and shifted SP in 11-AGNR, h) centered and shifted SP in 10-ZGNR. Insets: Unit cells for 11-AGNR and 10-ZGNR with the standard pore (*a* is the lattice constant of the supercell). From Ref. [76].

Although pristine GNRs can be metalic or semiconducting, their metallicity can be tunned by local changes of their morphology and edge chemistry [14, 38, 59–61, 164, 171, 176–181].

We begin our review by examining the band structures of porous armchair (AGNR) and zigzag (ZGNR) graphene nanoribbons, which are studied by large scale *ab-initio* DFT calculations [76]. We have used SIESTA 3.0 [182] in supercells of ($>$ 40 atoms), and neglected (in most cases) spin degrees of freedom. The calculations were done with the Perdew-Zunger LDA functional [183] and pseudopotentials with the cutoff energy of 400 Ry (double-zeta basis and polarization orbitals, 13 and 5 orbitals for C-atom and H-atom, respectively). See other details in Ref. [76].

All the GNRs are classified by the number of carbon dimers, N, that form the ribbon (N-GNR) [5]. As an example, we have studied the porous 11-AGNR and 10-ZGNR (both metallic when pristine), with the distances between nanopores of 12.78 Å and 12.3 Å, respectively, and elementary cells are shown in Figs. 12 (d, h). We have described PNCs perforated with pores of different shapes, sizes, and locations. Most of the results are obtained for arrays of

honeycomb-shaped pores, called the “standard pore" (SP) [90, 155], where in each pore six C atoms (one benzene ring) are excluded from the studied nanocarbon and the dangling bonds are terminated by hydrogens.

In Figs. 12 (a, b), one can see that the introduction of a periodic array of SPs in the center of 11-AGNR causes a significant band-gap opening ($0.15 - 0.92$ eV). On the other hand, both pristine and porous (same pores) 10-ZGNR have no energy band gap, as seen in Figs. 12 (e, f). When the SPs are displaced by one honeycomb cell towards the GNR-edge, the band gap in 11-AGNR shrinks ≈ 3.75 times, while 10-ZGNR remains metallic, as shown in Figs. 12 (c, g). We also checked that the PGNR band structures monotonously approach their pristine form as the separation between adjacent pores is increased. The densities of states (DOS) for the band structures presented are displayed in Figs. 12 (d, h).

The energy band gaps in ZGNRs and AGNRs are known to arise from a staggered sublattice potential and a quantum confinement [38, 60], respectively, and they depend on the ribbon width and its functionalization [166, 184, 185]. The wave functions of the HOMO and LUMO bands in AGNRs, which contribute directly to the area near E_f, are localized at the center of the ribbons, keeping their edges chemically stable [166]. In ZGNRs, these wavefunctions are localized at the ribbon edges. Consequently, when the SPs are positioned at the center of 11-AGNR a band gap opens in its band structure, while 10-ZGNR remains metallic. The metallicity of ZGNRs is caused by flat bands present at E_f, originating from highly localized states formed at the zigzag edges [166], as discussed below. When the pore is closer to the edge of 11-AGNR, its band structure is influenced less, while no significant change is observed in 10-ZGNR. These results can be generalized for other PGNRs provided that the pore is honeycomb like.

Porous graphene (PG)

Porous graphene (graphene antidot lattice) consists of a periodic arrangement of holes in a graphene sheet [167]. PG has been studied in a number of works [186–188], but in most studies hexagonal lattices of near-circular holes are considered [167–169]. Here, we use the $\{L, R\}$ PG superlattice classifaction [167] where L and R are measured in units of the graphene lattice constant $a = 2.46$ Å (see Fig. 13).

Various approaches have been used to describe the band structure of PGs. In TB approaches, a single-electron Schrödinger equation for an effective potential is solved. In the simplest version of TB, the Bloch wavefunctions are expanded over only localized atomic π orbitals of the carbon lattice atoms calculated with LCAO method and only nearest-neighbor overlap matrix elements are retained. These overlap matrix elements are regarded as emperical parameters fitted to the experimental data (e.g. the Fermi velocity). The DE can improve the bands close to their linear crossing points. In contrast to TB calculations, DFT approaches do not imply particle-hole symmetry around the Fermi level, as seen in Fig. 14.

The energy band gaps calculated in PG lattices by DE, TB and DFT methods are summarized in Table 15. The study of many different graphene antidot lattices disclosed a simple scaling law between their pore sizes and band gaps, $E_g = K\sqrt{N_{hole}}/N_{cell}$, where N_{hole} is the number of carbon atoms that have been removed from the pristine unit cell containing N_{cell} carbon atoms and $K \approx 25$ eV [167, 168]. Therefore, the band gaps increase with the increasing hole size and decreasing lattice constant.

http://dx.doi.org/10.5772/56247

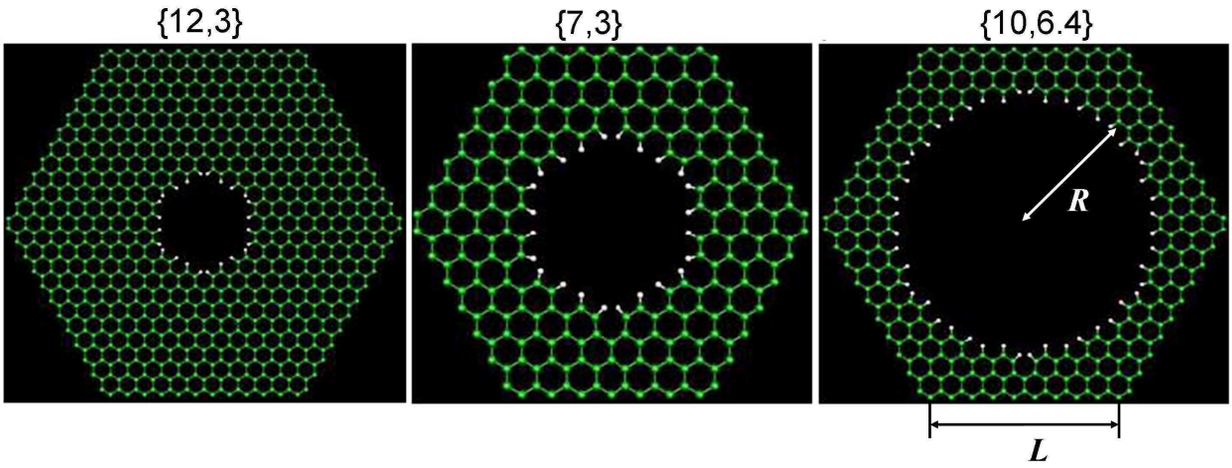

Figure 13. Unit cells of three hexagonal graphene antidot lattices with different side lengths L and hole radii R. The structures are denoted as L, R with both lengths measured in units of the graphene lattice constant $a \simeq 2.46$ Å. The edges of the holes have been hydrogen-passivated (hydrogen shown as white atoms). From Ref. [167].

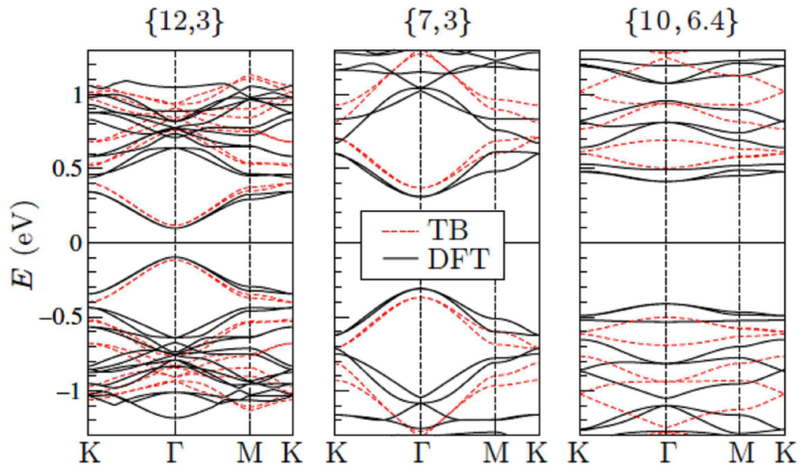

Figure 14. Band structures of three representative graphene antidot lattices. Full lines indicate results obtained using DFT, while TB results are shown with red dashed lines. From Ref. [167].

	{12, 3}		{7, 3}		{10, 6.4}	
	eV	$\Delta_{\{12,3\}}$	eV	$\Delta_{\{12,3\}}$	eV	$\Delta_{\{12,3\}}$
DE	0.54 (0.29)	1	1.27 (0.82)	2.35 (2.83)	1.53 (1.22)	2.83 (4.21)
TB	0.23	1	0.74	3.22	1.01	4.39
DFT	0.19	1	0.61	3.21	0.82	4.32

Figure 15. Band gaps of three representative graphene antidot lattices obtained by solving the DE, via TB, and using DFT. Values in parentheses are obtained using the DE. The band gaps are given in eV as well as in dimensionless values relative to the size of the band gap for the $\{L, R\} = \{12, 3\}$ structure [167].

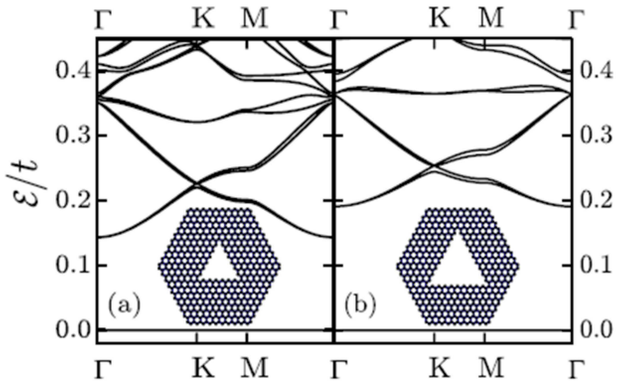

Figure 16. Band structure of an antidot lattice with triangular antidots calculated with TB method with $t \approx 2.8$ eV. Only bands above the Fermi level $\mathcal{E} = 0$ are shown. Γ, K, M stand for the high-symmetry points in the Brillouin zone. The flat band at the Fermi level is a) sixfold degenerate and b) ninefold degenerate. Adapted from Ref. [169].

The emergence of midgap energy states and corresponding quasi-flat bands around the Fermi level is another well pronounced effect related to the modification of the intact graphene lattice with nanopores. These states are relatively isolated, they have a minimal overlap of their wavefunctions, and thus they form flat bands. Graphene is known to be a bipartite lattice that can be divided into two sublattices A and B. According to the Lieb's theorem [189, 190], in a system where N_A and N_B are the total number of sites on the respective sublattices there should be $N_A - N_B$ zero energy states (so called, a global sublattice imbalance). The corresponding total magnetic moment per unit cell is just a half of this difference [167, 169].

In antidot graphene lattices, flat bands form at E_f due to the sublattice imbalance along the edges (zigzag GNRs) and pore rims. The electronic states corresponding to the zero energy flat bands (see Fig. 16) are predominantly localized in the vicinity of the pore rim (e.g. triangular pore). These localized states at zigzag rims were also studied in different types of pores, called "anti-molecules", where a set of simple rules was shown to link the net number of unpaired electrons with the degeneracy of flat bands [164, 167, 169, 174, 191]. It was shown that even a small number of zigzag-type of sites (local sublattice imbalance) per unit cell is enough to generate flat bands and related magnetism [176].

In previous studies, it was assumed that the perforation of graphene by nanopores opens up the energy band gap. The only exclusion from this trend was related to triangular pore shapes, due to their global sublattice imbalance. We have performed extensive *ab initio* calculations of electronic structures of PG-superlattices with different arrangements of the SPs [76]. SPs, largely used in our study, keep the global sublattice balance of the unit cell, but their short zigzag-like rims break the local balance and may still give rise to flat bands.

In Figs. 17 (a-d), we show the band structures of (edgeless) PGs with one honeycomb and three different rectangular SP-superlattices defined by N_A, N_Z, and displayed in Figs. 17 (e, f). Fig. 17 (g) also shows the studied rectangular superlattice with triangular-shape pores. The honeycomb SP-superlattice has flat bands around $E \approx -1.5$ eV (Fig. 17 a), which are absent in the rectangular SP-superlattices (Figs. 17 (b-d)). According to [169], such quasi-flat bands at non-zero energy might be ascribed to the local sublattice imbalance (globally $n_A = n_B$). However, the local sublattice imbalance due to SPs can not be the origin of flat bands in the band structure of the honeycomb SP-superlattice, since it has the same pores as the other

http://dx.doi.org/10.5772/56247

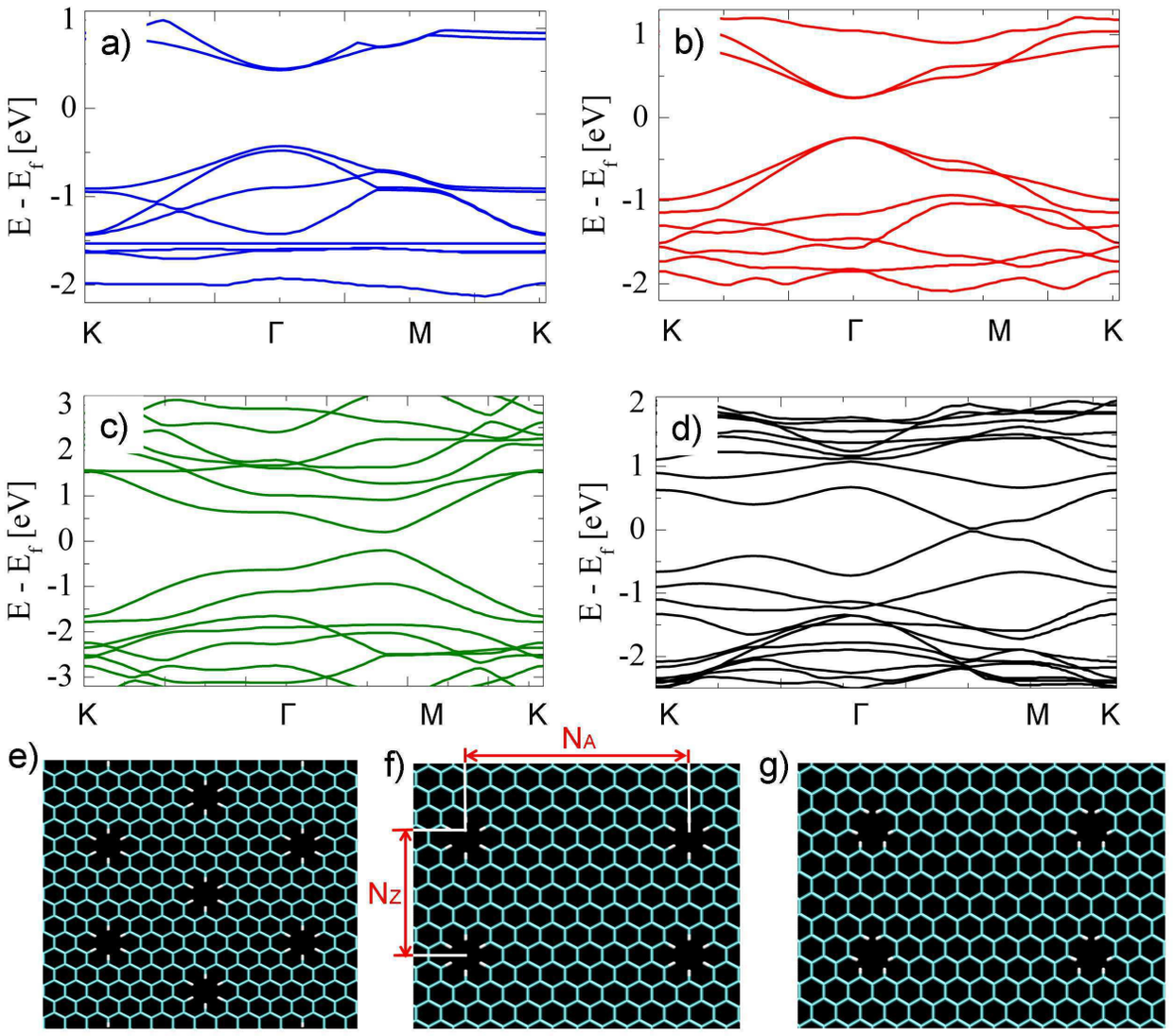

Figure 17. (top) Band structure of a) a honeycomb SP-superlattice in e) and three rectangular SP-superlattices with b) $N_A = 15$, $N_Z = 4$, c) $N_A = 7$, $N_Z = 2$, and d) $N_A = 7$, $N_Z = 8$. (bottom) e) honeycomb SP-superlattice, f) rectangular SP-superlattice characterized by N_A, N_Z, g) rectangular superlattice with triangular-shape pores. From Ref. [76] (see Fig. 16)

structures with no flat bands. Therefore, the flat bands are most likely related with the honeycomb SP-arrangement, which might produce differently localized states. These results show that the small number of zigzag sites at the very short SP-rim can not generate flat bands at the Fermi level or at its vicinity. In contrast, even the smallest triangular-shape pores break the global sublattice balance and generate an unbalanced π-electron density [175], associated with the appearance of rim-localized states and flat bands at E_f (compare with Fig. 16).

With these observations, we can now relate the band structures of PGNRs and PGs. Since SPs do not break the global sublattice balance in the PGNRs, their presence does not generate any new flat bands at E_f (see Fig. 12); on the contrary, we found that when AGNRs are perforated with triangular-shape pores, their band structure always contains flat bands at E_f. Even though the SPs do not create flat bands at E_f in GNRs, they still influence their band structure. While the band structures of AGNRs (Figs. 12 (b, c)) is influenced a lot, the

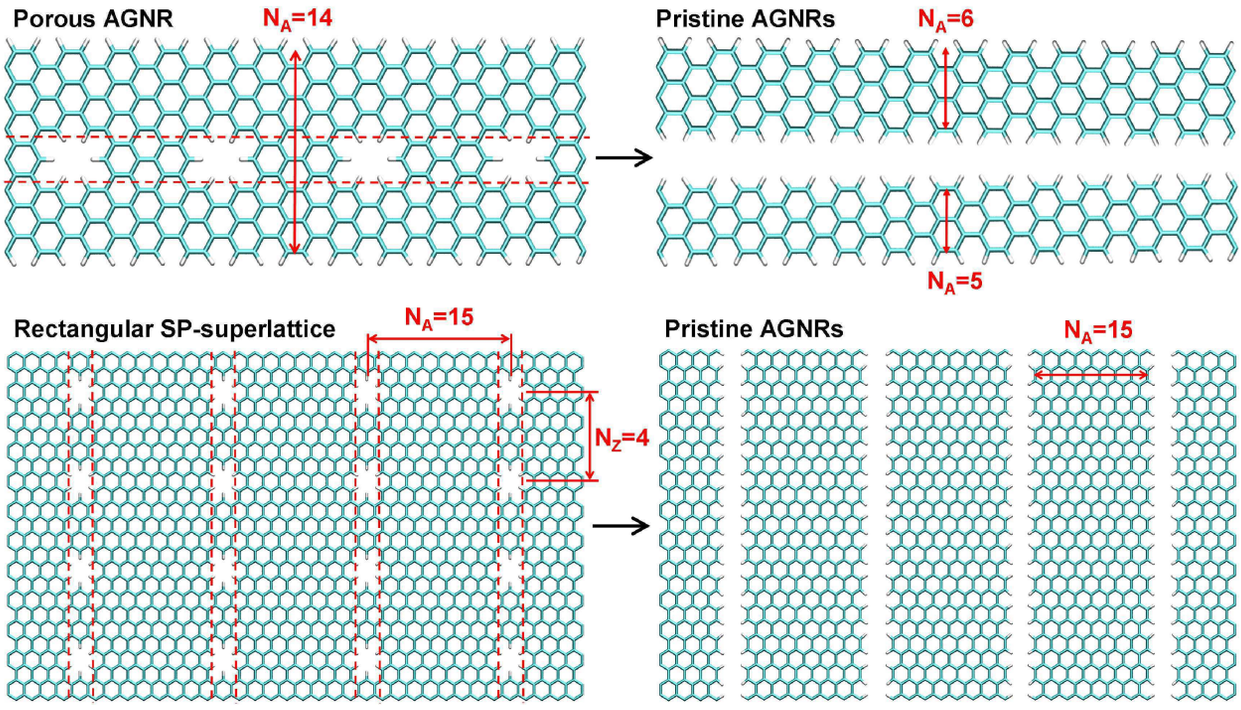

Figure 18. (top) Effective replacing of porous N-AGNR by "daughter" pristine N_1- and N_2-AGNR ($N = 14$, $N_1 = 5$, $N_2 = 6$). (bottom) Effective replacing of rectangular SP-superlattice with $N_A > N_Z$ by set of pristine AGNRs ($N_A = 15$, $N_Z = 4$). From Ref. [76].

band structures of ZGNRs with flat bands at E_f (local sublattice imbalance caused by zigzag edges) can not be significantly modified by SPs. Therefore, we conclude that all porous ZGNRs are metallic (checked by calculations).

Interestingly, we found that rectangular PG-superlattices perforated with SPs and larger pores of honeycomb symmetry can be both metallic and semiconducting [76]. It turns out that we can generalize these observations into a hypothesis that, in the first approximation, the electronic structure of these superlattices has the same type of conductivity as many parallel AGNRs or ZGNRs (of effective widths N_A or N_Z), depending on the ratio $\rho = N_A/N_Z$ (see Fig. 18 bottom). If $\rho \gg 1$, one can see the superlattice as being "cut" into separated N_A-AGNRs, while for $\rho \ll 1$ the same is true for separated N_Z-ZGNRs.

The above hypothesis was largely confirmed by our follow up calculations. For example, the conductivity in the PGs with $N_Z = 2$ is the same as in the corresponding AGNRs: metallic for $N_A = 5, 11, 17...$ and semiconducting for $N_A = 7, 9, 13, 15...$ (see also Table. 1). If we continue with the $N_A = 9, 15, 21, ...$ semiconducting AGNRs and increase the initially small $N_Z = 2$, we find that the PGs remain semiconducting for (roughly) $N_Z < N_A$, with the band gap shrinking with increasing N_Z, signaling the transition to the ZGNR-dominated metallic conductivity. If we continue with the the $N_A = 11$ metallic AGNRs, the PGs become metallic for all the N_Z, since the ZGNRs that take over at $N_Z > N_A$ are all metallic. Finally, when we continue from $N_A = 7, 13...$, the metallicity appears abruptly at $N_Z \geq 4$. In other cases, we expect that the transition between the AGNR and ZGNR-type of behavior occurs somewhere around the "diagonal", $\rho = 1$. Our calculations also show that the metal-semiconductor transitions predominantly occur in two regions of the Brillouin zones, as seen in Figs. 17 (b-d), and the bands can be partially flat in the k_y direction ($N_A = 7, 13, ..a.$).

http://dx.doi.org/10.5772/56247

Porous nanotubes

Unlike porous graphene and porous nanoribbons, the electronic structure of porous carbon nanotubes (PCNTs) was studied much less [173, 192]. However, there is a tight connection between CNTs and GNRs and clear correspondence between the electronic structures of pristine CNTs and structurally analogous GNRs. Moreover, the electronic structures of PNCs are similar to those of pristine GNRs [76].

We follow the Ezawa's notations [178] in description of GNRs and CNTs. While ZGNRs indexed by $\langle p,0\rangle$ are metallic for all p, only one third of AGNRs indexed by $\langle p,1\rangle$ are metallic. Since, only one half of AGNRs can be rolled into ZCNTs, only one third ZCNTs are metallic [178]. We found that this mapping can be generalized to the point that every metallic/semiconducting CNT corresponds to a metallic/semiconducting GNR. The unambiguous relationship can be expressed in terms of the chirality index, p, and the number of GNRs carbon dimers, N, as follows

$$\begin{aligned} \text{ZCNT}\langle p,0\rangle &\Rightarrow N\text{-AGNR}, \quad \text{where} \quad N = 2p+2\,, \\ \text{ACNT}\langle p,p\rangle &\Rightarrow N\text{-ZGNR}, \quad \text{where} \quad N = 2p+1\,. \end{aligned}$$

Intuitively, we can look at this CNT-GNR correspondence as a consequence of CNT "cutting" (Figs. 19 (top, middle)), which preserves the type of conductivity. The AGNRs and ZGNRs that do not match any CNTs are all semiconducting and metallic, respectively, as summarized in Table. 1.

AGNR <p,1>	dimers, N	7	8	9	10	11	12	13	14	ZGNR <p,0>	5	6	7	8	9	10	11	12
	p-index	4	5	6	7	8	9	10	11		4	5	6	7	8	9	10	11
	cond.	s	m	s	s	m	s	s	m		m	m	m	m	m	m	m	m
	geometry	s	a	s	a	s	a	s	a		a	s	a	s	a	s	a	s
ZCNT<(p+1)/2,0>	cond.		m		s		s		m	ACNT <p/2, p/2>	m		m		m		m	

Table 1. Correspondence rule for GNRs and CNTs. N - number of dimers forming GNR, p - index for the chirality vector in GNR and CNT; cond. - conductivity property (semiconducting (s) or metallic (m)); geometry defines the symmetry with respect to the mirror plane perpendicular to the ribbon and containing its axis: symmetric (s), asymmetric (a). Examples of AGNRs for $N = 7,...14$ and ZGNRs for $N = 5,...12$ are illustrated. From Ref. [76]

Analogously, porous CNTs might have band structures similar to porous GNRs. Tight-binding calculations predicted [173] that a line of SPs (separated by ~ 12.8 Å) should cause band gap opening in ACNTs, whereas porous ZCNTs should be semiconducting regardless of the pore shape. These results are in contradiction with our *ab-initio* calculations, which show that the metallicity of pristine ACNTs (Fig. 20 a) is preserved in the porous ACNTs (Fig. 20 e), even for triangular-shape pores with clear zigzag-like rims. In metallic ZCNTs, the SP-perforation causes band gap opening, as shown in Figs. 20 (b, f), while in semiconducting ZCNTs, it causes band gap shrinking, as seen in Figs. 20 (c, g).

The above observations allow us to build a *unified model* that can predict the type of conductivity in porous nanocarbons perforated with SPs and other pores that do not break the global sublattice balance. The model is based on the assumption that when nanocarbons (NCs) are perforated by a line of relatively close SPs, the type of conductivity in these PNCs is the same as in the (daughter) systems obtained from these nanocarbons by removing all C atoms within a stripe going in the direction of the pores and having the same width as the pores (all dangling C bonds are H-terminated). We call these modified NCs the daughter

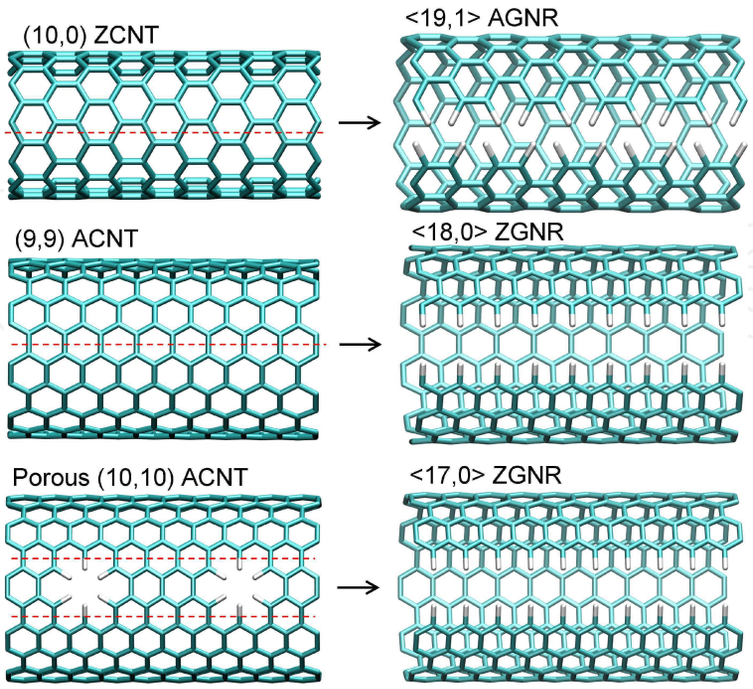

Figure 19. Cutting of: (top) (10,0)ZCNT into $\langle 19,1\rangle$AGNR and (middle) (9,9)ACNT into $\langle 18,0\rangle$ZGNR (opening of the GNRs is schematically shown). (bottom) Removal of atoms from porous (10,10)ACNT leading to $\langle 17,0\rangle$ZGNR. From Ref. [76].

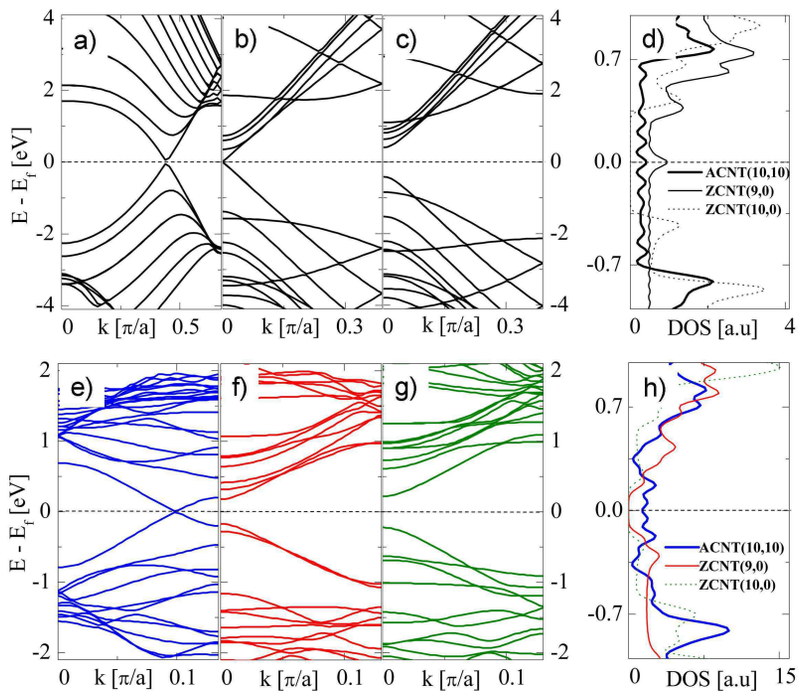

Figure 20. Band structures in pristine CNTs: a) ACNT (10,10), b) ZCNT (9,0), c) ZCNT (10,10); d) DOS. Porous CNTs: e) ACNT (10,10), f) ZCNT (9,0), g) ZCNT (10,10); h) DOS. The energy scales for (b,c) and (f,g) cases are the same. From Ref. [76].

systems of the original NCs (two GNRs for PGNRs, one GNR for PCNTs, and a GNR-lattice for PG). This rule predicts that: (1) Porous ACNTs are metallic as the (daughter) ZGNRs; Fig. 19 (bottom) shows effective replacing of porous ACNT by pristine ZGNR. Perforating the resulting ZGNRs (and the other half of ZGNRs that can not be rolled up into CNTs) gives two metallic ZGNRs, preserving the ZGNR-metallicity. (2) Porous ZCNTs may give semiconducting or metallic AGNRs. Cutting all the AGNRs may give pairs of AGNRs with any conductivity. These results were confirmed by *ab initio* calculations.

We now use these rules to predict metallicity in porous AGNRs with SPs. We assume that their band gaps are $E_{BG} \simeq \min(E_{1BG}; E_{2BG})$, where E_{1BG}, E_{2BG} are band gaps of their two daughter AGNRs (see Fig. 18 (top)). With this inference, we can derive an analytical expression describing the dependence of the band gap on the width of the porous AGNRs. For simplicity, we consider SPs positioned in the middle of AGNRs of the width of $W = a\sqrt{3}(N-1)/2$, where a is the C-C distance and N is the number of dimers. By evaluating the widths of the pristine daughter AGNRs, we find that porous N-AGNRs are potentially metallic if the number of C-C dimers is given by at least one of these equations

$$N = \left(6k + 11 + (-1)^k\right)/2\,, \quad N = 6k + 3 + 2(-1)^k\,,$$
$$N = 12k + 9, \quad (k = 0, 1, 2...)\,, \tag{1}$$

i.e., if $N = 5, 6, 7, 8, 9, 12, 14, 17, 18, 19, 20, ...$ In Fig. 21 (top), we compare the *ab-initio* energy band gaps in pristine [59, 180] and porous AGNRs to validate the above model. In contrast to the pristine ribbons, where the metallic points emerge with the period of 3, ($N_{met} = 3m + 2$), the band gaps of porous AGNRs have a more complex dependence. Nevertheless, the positions of the band gap minima agree with Eqn. 1.

We can extend the assumptions used in Eqn. 1 to PNCs perforated with larger and shifted honeycomb-like pores. Their presence may still be reduced to removing from the AGNRs a layer of atoms of the width given by the pore size, where the minimum band gap of the two resulting AGNRs can determine the band gap of the porous AGNR. For example, when the SP is shifted in the 11-AGNR by one honeycomb from the ribbon center, the two daughter pristine 4-AGNRs are replaced by 2-AGNR and 6-AGNR (all semiconducting). This should lead to a band gap shrinkage, in agreement with our *ab-initio* calculations, presented in Figs. 12 (b, c). Alternatively, we can replace the SP by a double-size hexagonal pore with 24 C-atom excluded. If the 11-AGNR and 12-AGNR are perforated by such pores, they become semiconducting, since their cutting leads to semiconducting 2-AGNRs and 2- and 3-AGNR, respectively. These results are in agreement with *ab-initio* calculations, giving in 11-AGNR and 12-AGNR the band gaps of 1.1 eV and 1.18 eV, respectively. We have also tested the triple-size hexagonal pore (54 C-atoms excluded) in order to check how its long rims affect band structure of GNRs. Our calculations show that no additional features (e.g. flat bands at the Fermi level) appear when the GNR are perforated by these pores. In contrast, when these AGNRs are perforated with SPs in the ribbon center, only the 11-AGNR is semiconducting.

Finally, we discuss porous ZCNTs that can have any conductivity. In Fig. 21 (bottom), we present the energy band gap of porous ZCNTs in dependence on the chirality index, p. It exhibits similar periodicity as in the pristine ZCNTs. However, the model is not reliable in porous ZCNTs. For example, the porous ZCNT(7,0) and ZCNT(8,0) have band gaps similar

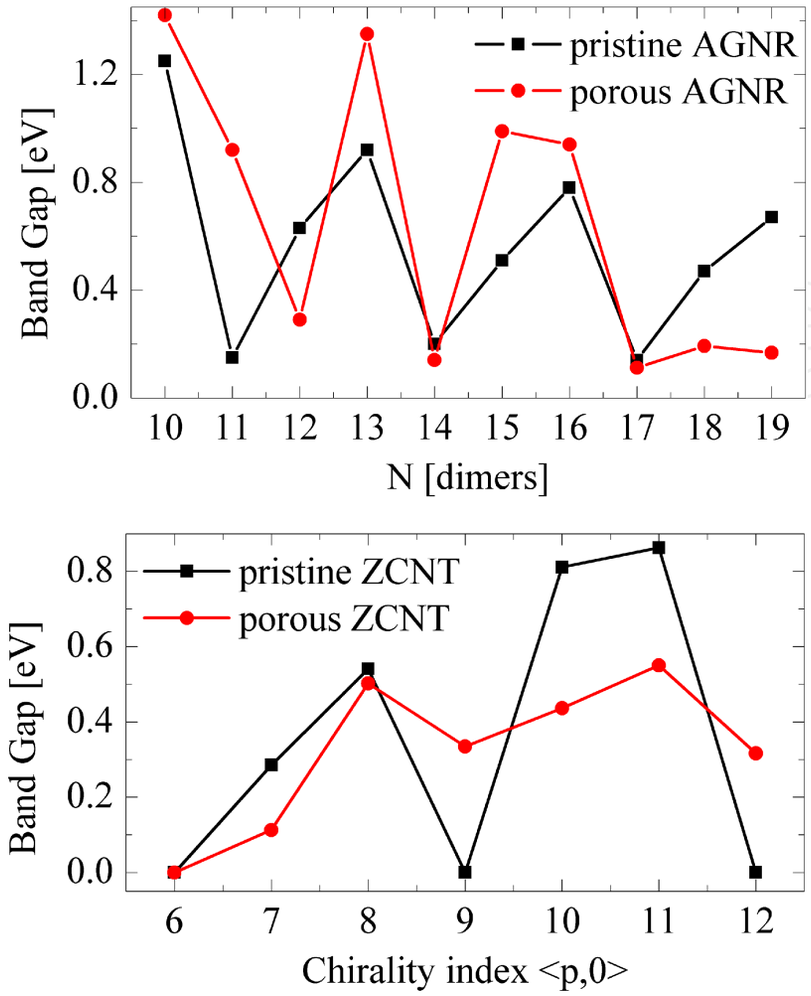

Figure 21. (top) Dependence of the band gap in the pristine and porous AGNR on the number of dimers (the central position of the SP). (bottom) The same dependence in ZCNT on the chirality index. From Ref. [76].

to the daughter 11-AGNR and 13-AGNR, respectively. But the same is not true for the porous ZCNT(9,0) and ZCNT(10,0) paired with the daughter 15-AGNR and 17-AGNR, respectively. In principle, this failure might be caused by the fact that the AGNRs are not calculated deformed as the corresponding daughter ZCNTs [193, 194]. However, our calculations show that the bent 17-AGNR has almost the same band gap as the pristine 17-AGNR. Therefore, a more quantitative approach needs to be used here.

It is of interest to see if other types of periodic modifications can also be used to tune the band structures of nanocarbons. To briefly examine this idea, we have replaced SPs by Stone-Wales 55-77 defects [195]. In Fig. 22, we show the band structures of 11-AGNR, 10-ZGNR, and graphene superlattices modified in this way. The periodic array of SW 55-77 defect in 11-AGNR leads to small bang gap opening, as shown Fig. 22 (a), in analogy to 11-AGNR with SPs (Fig.12 b). The band structure of 10-ZGNR, shown in Fig. 22 (b), is not sensitive to this perturbation, as in the SP-perturbations (Fig.12 f). On the other hand, when we replace in graphene superlattices SPs with the SW 55-77 defects, we can obtain qualitatively different band structures. In particular, the band structure of graphene modified by SW 55-77 defects in the array with $N_A = 7$ and $N_Z = 4$ (Fig. 22 c) is similar to that of the SP-superlattice with the same N_A and N_Z, but here we also observe opening of a small band gap. In Fig. 22 (d),

http://dx.doi.org/10.5772/56247

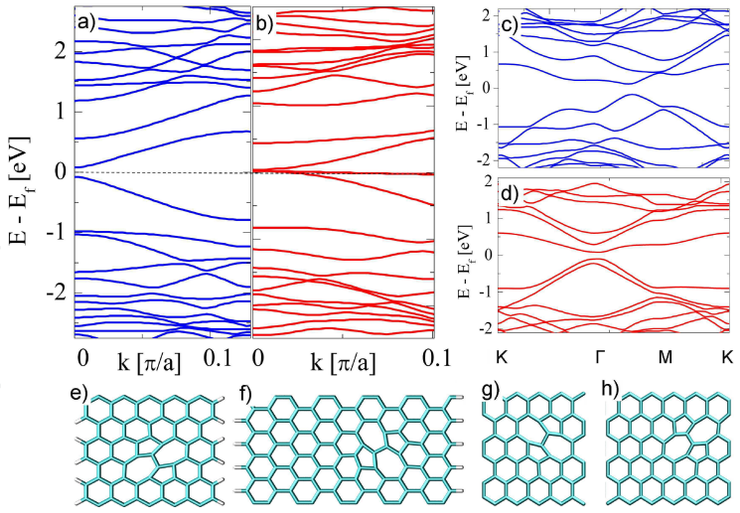

Figure 22. Band structures of nanocarbons with periodic 55-77 Stone-Wales defects: a) 11-AGNR, b) 10-ZCNT, c) graphene superlattice with $N_A = 7$ and $N_Z = 4$, d) graphene superlattice with $N_A = 9$ and $N_Z = 4$. Figures (e-h) show unit cells for the respective cases. From Ref. [76].

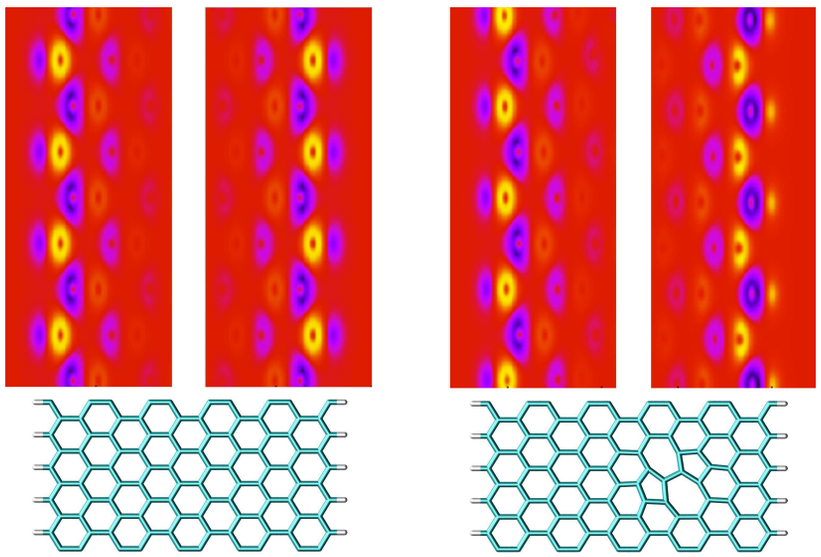

Figure 23. 10-ZGNR edge magnetism. The alternation of spin imbalance as result of introduction of 55-77 SW defects. From Ref. [76].

we show the band structure of the SW-graphene superlattice ($N_A = 9$ and $N_Z = 4$), which is semiconducting as the PG-superlattice with the same N_A and N_Z. These observations show that periodic defects could also be used to tune band gaps in nanocarbons, but the rules might be slightly different.

For completeness, we have recalculated some of the above structures including spin polarization (we used a set of LDA and GGA functionals). It turns out, the band structures of nanocarbons can be modified by the spin polarization (zigzag edges) [164], but the presence of SPs does not introduce additional magnetic features beyond the changes described already in the non-magnetic calculations. Interestingly, the presence of arrays of SW (55-77) defects in ZGNRs can alternate mutual orientation of the magnetic moments localized at the opposite edges, due to topological changes in the sublattices, as shown in Fig. 23.

We have shown that the formation of nanopores in PNCs can lead to the appearance of band gaps, midgap states and quasi-flat bands around the Fermi level. We have discussed a unified picture of electronic structures in PNCs, where the formation of periodic arrays of nanopores can be regarded as an effective cutting. We have also seen that nanopores can induce a local spin imbalance related to a non-zero magnetic moment. All these effects show that the electronic parameters of PNCs are highly tunable, which can be used in numerous potential applications.

Additional control of the electronic structure in PNCs

The electronic structure of PNCs can be further influenced and controlled by the chemistry of the edges and pore rims, various defects, mechanical deformations, etc. For example, it was shown that hydrogen adsorbate structures on graphene are thermodynamically stable well above the room temperature, and the resulting band gap opening is stable against a weak disorder [165, 185]. Extensive studies of GNRs and PGNRs with chemically functionalized edges were carried on [166, 184]. It was shown that edge or bulk functionalization or atomic substitution in PNCs (n/p doping) is an efficient mean to change electronic characteristics of nanocarbons. In particular, chemical functionalization of zigzag-type of edges breaks the spin degeneracy, as shown in Fig. 24 [166]. It promotes a metal-semiconductor transition or a half-semiconducting state with two spin channels (spin-dependent band gap or opposite spin polarizations in the valence and conduction bands).

An edge functionalization of AGNRs does not lift the spin degeneracy and it can generate electronic states within a few eV away from the Fermi level in the valence band with no effect on their energy band gap [166]. Substitutions of carbon atoms with N and B atoms can produce various effects, depending on the position of the substitutional site [166]. In particular, edge substitutions at low density do not significantly alter the band gap, while bulk substitutions promote the onset of metal-semiconductor transitions, as shown in Fig. 25 [166].

Mechanical deformations, such as application of uniaxial or shear strains and out-of-plane deformation or bending, can also modify the energy band gap. Compared to a graphene sheet where the band gap remains close to zero even if a large strain is applied, the band gap of GNRs and PGNRs depends strongly on their edge shape [194]. For AGNRs, a weak uniaxial strain changes the band gap in a linear fashion, whereas a large strain results in periodic oscillation of the band gap. In contrast, the shear strain always reduces the band gap. In ZGNRs, a strain changes the spin polarization at the edges, and thereby modulate the band gap. Out-of-the-plane radial deformations can cause a semiconductor-metal transition in GNRs, due to the hybridization of σ and π orbitals and modifications of orbital interactions [193]. Mechanical deformations may also be related with other interesting phenomena, such as a piezoelectricity in a boron-nitride analogue of graphene [196].

4.2. Electron transport in porous nanocarbons

Electronic structures in graphene-based systems determine their electronic transport properties. Specifically, electronic transmission through such systems under bias (current-voltage characteristics) strongly depends on their energy band gap, densities of states, bands lineup, spin states, and the reciprocal positions of an Fermi energy level of their electrodes with respect to their HOMO and LUMO bands [197–199].

http://dx.doi.org/10.5772/56247

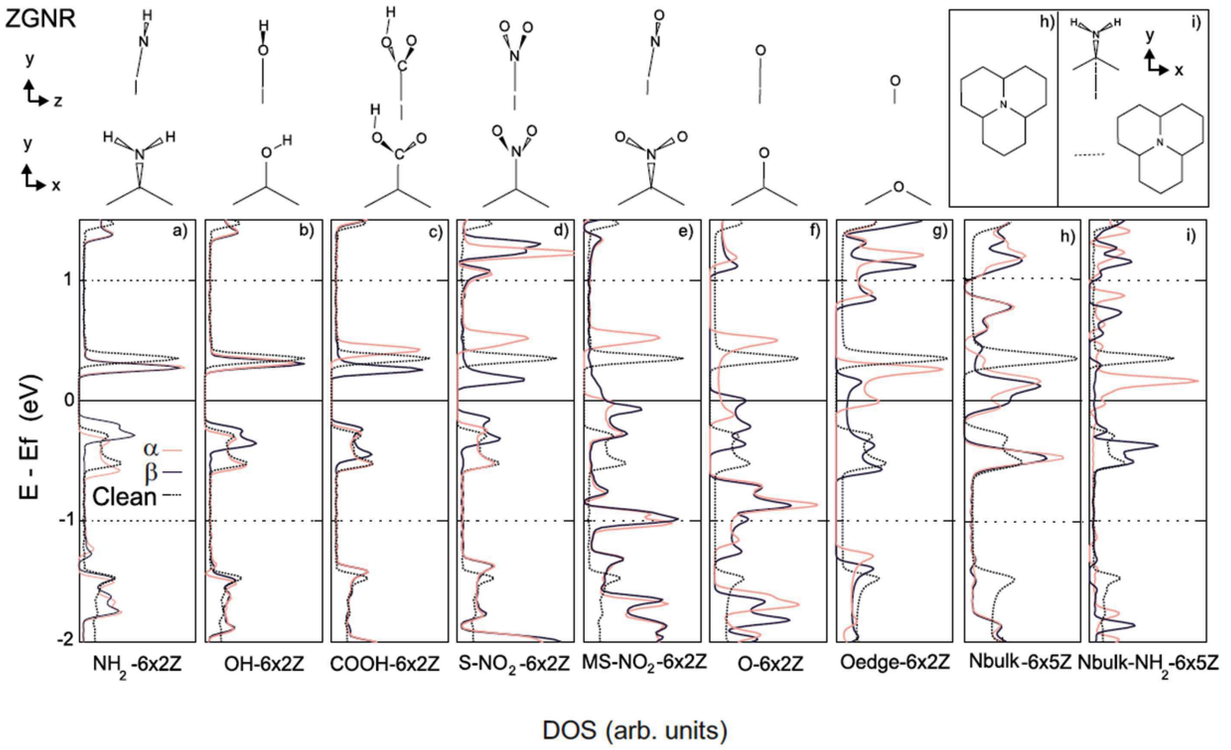

Figure 24. Spin density of α (red solid line) and β (black solid line) for functionalized ZGNRs in comparison with a clean ribbon (black dotted line). 6-ZGNR functionalized with a) NH_2, b) OH, c) COOH, d) stable-NO_2, e) metastable-NO_2 and f) O radicals in one of the ribbon edges, resulting in (a)-(f) lifting of the spin degeneracy, (a)-(d) spin-selective band gap, or (e) and (f) semiconductor-metal transition. g) Oxygen edge substitutional atom favoring a semiconductor-metal transition. (h) 6-ZGNR with a nitrogen bulk substitution in the center of the ribbon. i) Nitrogen bulk substituted ribbon shown in h) with an extra single NH_2 at the edge of the opposite carbon sublattice, with the maximum distance between N and NH_2 in the periodic direction, resulting in a semiconductor-metal transition. From Ref. [166].

The quantum transport in biased graphene nanoribbons (GNRs) was extensively studied [48, 200–202]. For example, it was shown that spin-valve devices based on GNRs can exhibit magnetoresistance values that are thousands of times higher than previously reported experimental values [203]. GNR doping was shown to significantly affect their transport properties [48, 199, 204]. Modeling of electron transport in GNRs was done using the Landauer-Buttiker formalism [205], non-equilibrium Green's function (NEGF) techniques [206], and other methods.

In Fig. 26, we show the calculated quantum conductances of two pristine armchair GNRs of different widths and a pristine zigzag GNR in anti-ferromagnetic and ferromagnetic states [200]. One can see that the energy band gap of armchair GNRs depends on the ribbon widths. The step-like behavior of the transmission spectrum is related with the available conductance channels (bands) [201]. In zigzag GNRs, the electron transport is dominated by edge states which are spin-polarized. Depending on the edge spin configuration ($\uparrow\downarrow$ or $\uparrow\uparrow$) the zigzag GNRs are predicted to be semiconducting or semi-metallic, which is reflected in the presence or absence of the energy interval of zero transmission, respectively.

We have calculated by NEGF techniques the electron transmission through porous armchair GNRs. The system setup and the electron transmission spectra are shown in Fig. 27. As one can see, the perforation of 11-AGNR with a pore can significantly affect its conductance.

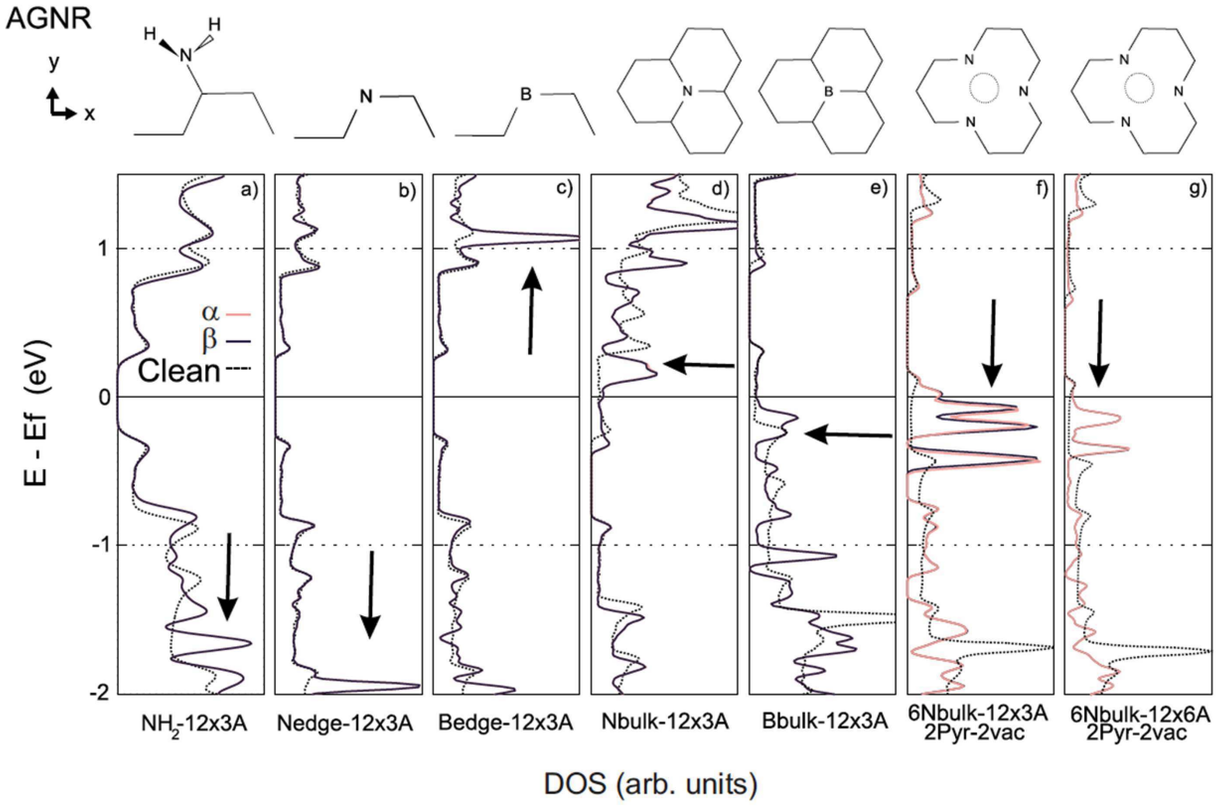

Figure 25. Spin density of α (red solid line) and β (black solid line) for functionalized AGNRs in comparison with a clean ribbon (black dotted line). 12-AGNR functionalized with a) NH_2, b) N, c) B edge substitutional atoms, N and B bulk substitutions are shown in d) and e), where a semiconductor-metal transition occurs. f) and g) Two pyridinelike substitutional doping in the bulk resulting in a metallic behavior. Arrows indicate impurity levels due to substitutional atoms. The DOS of the clean ribbon is shifted for the bulk N and B substitutions, so that the edges of the valence band of clean and doped ribbons coincide. From Ref. [166].

The most pronounced effect is the emergence of additional regions of zero transmission that proves its dependence on the pore position. The plausible reason of this effect is the quantum interference [207] between different spatial paths that electrons can follow in the scattering region. Such a sensitivity may be used for molecular passage detection via electric measurements.

5. Conclusions

In the last decade, intensive research of graphene, its precursors and derivatives revealed the great potential of nanocarbons. These materials have unique mechanical, chemical and electronic properties. Modulating the atomic structure of nanocarbons with chemically functionalized nanopores was found to be an efficient way to impart to them the desired properties and functions. The spectrum of nanocarbon applications can cover electronics, optics, and materials for general use, such as molecular filtration, sensing, detection, and recognition. In electronics, we should mention that perforation of nanocarbons with nanopores can not only trigger a metal-semiconductor transition but also a subtle magnetic phase transition, making porous nanocarbons promising materials for spin current filters and magnetoresistors. When it comes to molecular sensing and detection, one can use the exceptional sensitivity of PNC electronic structures to the presence of molecules and

http://dx.doi.org/10.5772/56247

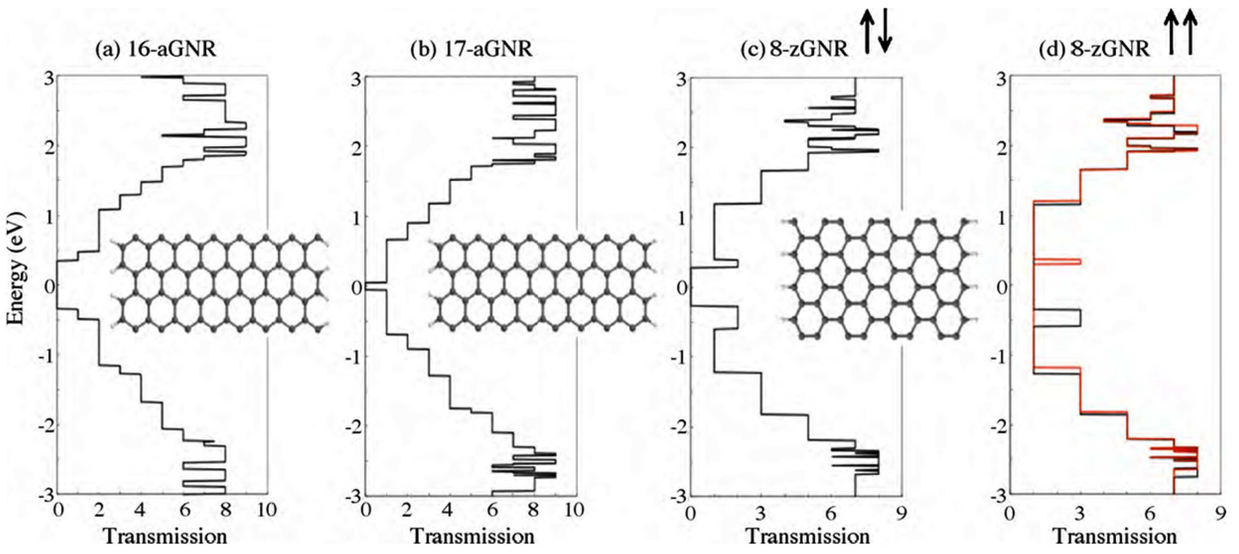

Figure 26. Quantum transport in graphene nanoribbons at zero bias. Atomic structures and electronic transmission of (a) 16-armchair GNR; (b) 17-armchair GNR, 8-zigzag GNR with (c) anti-parallel or (d) parallel spin orientations between the two magnetic edges. The spin-dependent transport is evaluated for both magnetic configurations of the 8-zGNR (c and d) but is only visible for the parallel spin orientations (ferromagnetic one). In such case, one spin orientation is labeled majority-spin (in black) while the other is labeled minority-spin (in red). Adapted from Ref. [200].

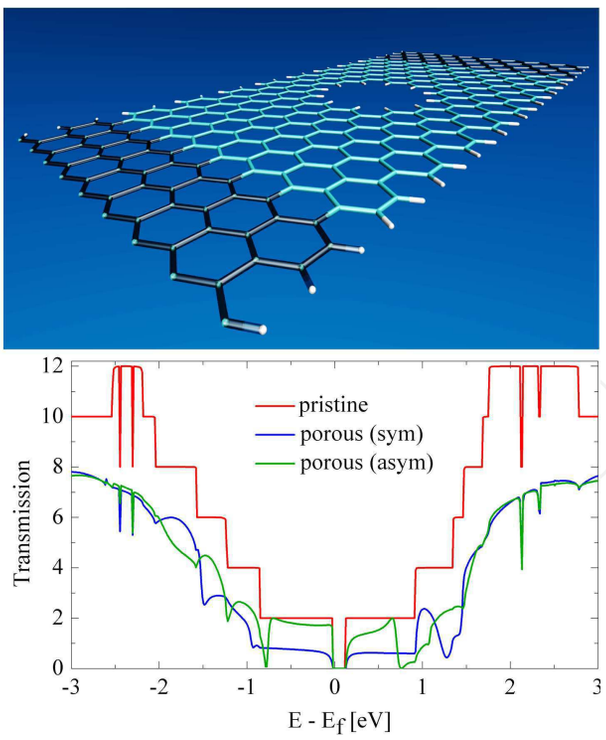

Figure 27. Quantum transport in 11-AGNR (see inset in Fig. 12) at zero bias. (top) Schematic view of two-probe porous AGNR with edges passivated by hydrogen atoms. Central scattering region, left and right electrodes are indicated. (bottom) Electron transmission spectra for the pristine 11-AGNR, 11-AGNR with centered pore, 11-AGNR with shifted pore.

passage through their pores. However, in order to benefit from material properties of porous nanocarbons more research is needed in the preparation of atomically precise porous nanocarbons.

Acknowledgments

A.B. would like to acknowledge the support of the Paaren Graduate Fellowship from the Department of Chemistry at the University of Illinois at Chicago. This work was partially supported by a grant from ACS PRF 53062. The simulations and other calculations have been realized with the NERSC, NCSA and CNM supercomputer networks.

Author details

Boyang Wang[1], Artem Baskin[2] and Petr Král[2,3,⋆]

⋆ Address all correspondence to: pkral@uic.edu

1 Institute of Chemistry, Chinese Academy of Science, Beijing, R.P. China
2 Department of Chemistry, University of Illinois at Chicago, IL, USA
3 Department of Physics, University of Illinois at Chicago, IL, USA

References

[1] Novoselov K. S. Geim A. K. Morozov S. V. Jiang D. Zhang Y. Dubonos S. V. Grigorieva I. V. Firsov A. A. Electric Field Effect in Atomically Thin Carbon Films, *Science* 2004; *306*, 666–669.

[2] Lenosky T. Gonze X. Teter M. Elser V. Energetics of negatively curved graphitic carbon, *Nature* 1992; *355*, 333–335.

[3] Castro Neto A. Guinea F. Peres N. Novoselov K. Geim A. The electronic properties of graphene, *Rev. Mod. Phys.* 2009; *81*, 109–162.

[4] Abergel D. S. L. Russell A. Fal'ko V. I. Visibility of graphene flakes on a dielectric substrate, *Appl. Phys. Lett.* 2007; *91*, 063125.

[5] Cresti A. Nemec N. Biel B. Niebler G. Triozon F. Cuniberti G. Roche S. Charge transport in disordered graphene-based low dimensional materials, *Nano Research* 2008; *1*, 361–394.

[6] Freitag M. Graphene: Nanoelectronics goes flat out, *Nat Nano* 2008; *3*, 455–457.

[7] Katsnelson M. I. Novoselov K. S. Geim A. K. Chiral tunnelling and the Klein paradox in graphene, *Nat Phys* 2006; *2*, 620–625.

[8] Hwang E. H. Adam S. Das Sarma S. Carrier Transport in Two-Dimensional Graphene Layers, *Phys. Rev. Lett.* 2007; *98*, 186806.

[9] Peres N. Guinea F. Castro Neto A. Electronic properties of two-dimensional carbon, *Annals of Physics* 2006; *321*, 1559–1567.

[10] Gusynin V. P. Sharapov S. G. Unconventional Integer Quantum Hall Effect in Graphene, *Phys. Rev. Lett.* 2005; *95*, 146801.

[11] Novoselov K. S. Geim A. K. Morozov S. V. Jiang D. Katsnelson M. I. Grigorieva I. V. Dubonos S. V. Firsov A. A. Two-dimensional gas of massless Dirac fermions in graphene, *Nature* 2005; *438*, 197–200.

[12] Datta S. Strachan D. Khamis A., S.M. anf Johnson Crystallographical etching of few layer graphene, *Nano Lett.* 2008; *8*, 1912–1915.

[13] Campos-Delgado J. e. a. Bulk production of new form of sp(2) carbon: crystalline graphene nanoribbons, *Namo Lett.* 2008; *8*, 2773–2778.

[14] Yang X. e. a. Two-dimensional graphene nanoribbons, *J. Am. Chem. Soc.* 2008; *130*, 4216–4217.

[15] Li W., X.L. X.R. L., Zhang Lee S. Dai H. Chemically derived, ultrasmooth graphene nanoribbon semiconductors, *Science* 2008; *319*, 1229–1232.

[16] Chen Z. Lin Y. Rooks M. Avouris P. Graphene nano-ribbon electronics, *Phisica E* 2007; *40*, 228–232.

[17] Han M. Ozyilmaz B. Zhang Y. Kim P. Energy band-gap engineering of graphene nanoribbons, *Phys. Rev. Lett.* 2007; *98*, 206805.

[18] Yan L. Zheng Y. Zhao F. Li S. Gao X. Xu B. Weiss P. Zhao Y. Chemistry and physics of a single atomic layer: strategies and challenges for functionalization of graphene and graphene-based materials, *Chem Soc Rev.* 2012; *41*, 97–114.

[19] Kuila T. Bose S. Mishra A. K. Khanra P. Kim A. N. H. Lee J. H. Chemical functionalization of graphene and its applications, *Prog. Mater. Sci.* 2012; *57*, 1061–1105.

[20] Georgakilas V. Otyepka M. Bourlinos A. B. Chandra V. Kim N. Kemp K. C. Hobza P. Zboril R. Kim K. S. Functionalization of Graphene: Covalent and Non-Covalent Approaches, Derivatives and Applications, *Chem. Rev.* 2012; *112*, 6156–6214.

[21] Sreejith S. Ma X. Zhao Y. Graphene Oxide Wrapping on Squaraine-Loaded Mesoporous Silica Nanoparticles for Bioimaging, *J. Am. Chem. Soc.* 2012; *134*, 17346–17349.

[22] Yang J. Heo M. Lee H. J. Park S.-M. Kim J. Y. Shin H. S. Reduced Graphene Oxide (rGO)-Wrapped Fullerene (C60) Wires, *ACS Nano* 2011; *5*, 8365–8371.

[23] Wang S. Manga K. K. Zhao M. Bao Q. Loh K. P. Wrapping Graphene Sheets Around Organic Wires for Making Memory Devices, *Small* 2011; *7*, 2372–2378.

[24] Lomeda J. R. Doyle C. D. Kosynkin D. V. Hwang W.-F. Tour J. M. Diazonium Functionalization of Surfactant-Wrapped Chemically Converted Graphene Sheets, *J. Am. Chem. Soc.* 2008; *130*, 16201–16206.

[25] Dikin D. A. Stankovich S. Zimney E. J. Piner R. D. Dommett G. H. B. Evmenenko G. Nguyen S. T. Ruoff R. S. Preparation and characterization of graphene oxide paper, *Nature* 2007; *448*, 457–460.

[26] Eda G. Fanchini G. Chhowalla M. Large-area ultrathin films of reduced graphene oxide as a transparent and flexible electronic material, *Nat Nano* 2008; *3*, 270–274.

[27] Chen D. Feng H. Li J. Graphene Oxide: Preparation, Functionalization, and Electrochemical Applications, *Chem. Rev.* 2012; *112*, 6027–6053.

[28] Campos L. C. Manfrinato V. R. Sanchez-Yamagishi J. D. Kong J. Jarillo-Herrero P. Anisotropic Etching and Nanoribbon Formation in Single-Layer Graphene, *Nano Lett.* 2009; *9*, 2600–2604.

[29] Wang X. Dai H. Etching and narrowing of graphene from the edges, *Nat Chem* 2010; *2*, 661–665.

[30] Boukhvalov D. W. Katsnelson M. I. Chemical Functionalization of Graphene with Defects, *Nano Lett.* 2008; *8*, 4373–4379.

[31] Yang H. Shan C. Li F. Han D. Zhang Q. Niu L. Covalent functionalization of polydisperse chemically-converted graphene sheets with amine-terminated ionic liquid, *Chem. Commun.* 2009; *9*, 3880–3882.

[32] Quintana M. Spyrou K. Grzelczak M. Browne W. R. Rudolf P. Prato M. Functionalization of Graphene via 1,3-Dipolar Cycloaddition, *ACS Nano* 2010; *4*, 3527–3533.

[33] Cui X. Zhang C. Hao R. Hou Y. Liquid-phase exfoliation, functionalization and applications of graphene, *Nanoscale* 2011; *3*, 2118–2126.

[34] Englert J. M. Dotzer C. Yang G. Schmid M. Papp C. Gottfried J. M. Steinrück H.-P. Spiecker E. Hauke F. Hirsch A. Covalent bulk functionalization of graphene, *Nat Chem* 2011; *3*, 279–286.

[35] Bai H. Xu Y. Zhao L. Li C. Shi G. Non-covalent functionalization of graphene sheets by sulfonated polyaniline, *Chem. Commun.* 2009; *3*, 1667–1669.

[36] Cui Y. Kim S. N. Jones S. E. Wissler L. L. Naik R. R. McAlpine M. C. Chemical Functionalization of Graphene Enabled by Phage Displayed Peptides, *Nano Lett.* 2010; *10*, 4559–4565.

[37] Lin Q. Chen Y. H. Wu J. B. Kong Z. M. Effect of N-doping on band structure and transport property of zigzag graphene nanoribbons, *Act. Phys. Sin.* 2011; *60*, 097103.

[38] Sols F. Guinea F. Neto A. H. C. Coulomb Blockade in Graphene Nanoribbons, *Phys. Rev. Lett.* 2007; *99*, 166803.

[39] Hod O. Peralta J. E. Scuseria G. E. Edge effects in finite elongated graphene nanoribbons, *Phys. Rev. B* 2007; *76*, 233401.

[40] Lee E. J. H. Balasubramanian K. Weitz R. T. Burghard M. Kern K. Contact and edge effects in graphene devices, *Nat Nano* 2008; *3*, 486–490.

[41] Castro E. V. Peres N. M. R. Santos Lopes dos J. M. B. Neto A. H. C. Guinea F. Localized States at Zigzag Edges of Bilayer Graphene, *Phys. Rev. Lett.* 2008; *100*, 026802.

[42] Ritter K. A. Lyding J. W. The influence of edge structure on the electronic properties of graphene quantum dots and nanoribbons, *Nat Mater* 2009; *8*, 235–242.

[43] Liu Z. Suenaga K. Harris P. J. F. Iijima S. Open and Closed Edges of Graphene Layers, *Phys. Rev. Lett.* 2009; *102*, 015501.

[44] Kudin K. N. Zigzag Graphene Nanoribbons with Saturated Edges, *ACS Nano* 2008; *2*, 516–522.

[45] Rutter G. M. Guisinger N. P. Crain J. N. First P. N. Stroscio J. A. Edge structure of epitaxial graphene islands, *Phys. Rev. B* 2010; *81*, 245408.

[46] Liu Y. Dobrinsky A. Yakobson B. I. Graphene Edge from Armchair to Zigzag: The Origins of Nanotube Chirality, *Phys. Rev. Lett.* 2010; *105*, 235502.

[47] Jiang D.-e. Sumpter B. G. Dai S. Unique chemical reactivity of a graphene nanoribbon's zigzag edge, *J. Chem. Phys.* 2007; *126*, 134701.

[48] Yan Q. Huang B. Yu J. Zheng F. Zang J. Wu J. Gu B.-L. Liu F. Duan W. Intrinsic Current Voltage Characteristics of Graphene Nanoribbon Transistors and Effect of Edge Doping, *Nano Lett.* 2007; *7*, 1469–1473.

[49] Gunlycke D. Li J. Mintmire J. W. White C. T. Edges Bring New Dimension to Graphene Nanoribbons, *Nano Lett.* 2010; *10*, 3638–3642.

[50] Sun Z. Kohama S.-i. Zhang Z. Lomeda J. Tour J. Soluble graphene through edge-selective functionalization, *Nano Res.* 2010; *3*, 117–125.

[51] Xie L. Ling X. Fang Y. Zhang J. Liu Z. Graphene as a Substrate To Suppress Fluorescence in Resonance Raman Spectroscopy, *J. Am. Chem. Soc.* 2009; *131*, 9890–9891.

[52] Ambrosi A. Bonanni A. Pumera M. Electrochemistry of folded graphene edges, *Nanoscale* 2011; *3*, 2256–2260.

[53] Begliarbekov M. Sasaki K.-I. Sul O. Yang E.-H. Strauf S. Optical Control of Edge Chirality in Graphene, *Nano Lett.* 2011; *11*, 4874–4878.

[54] Suenaga K. Koshino M. Atom-by-atom spectroscopy at graphene edge, *Nature* 2010; *468*, 1088–1090.

[55] Gupta A. K. Russin T. J. Gutiérrez H. R. Eklund P. C. Probing Graphene Edges via Raman Scattering, *ACS Nano* 2009; *3*, 45–52.

[56] Casiraghi C. Hartschuh A. Qian H. Piscanec S. Georgi C. Fasoli A. Novoselov K. S. Basko D. M. Ferrari A. C. Raman Spectroscopy of Graphene Edges, *Nano Lett.* 2009; *9*, 1433–1441.

[57] Bell D. C. Lemme M. C. Stern L. A. Williams J. R. Marcus C. M. Precision cutting and patterning of graphene with helium ions, *Nanotechnology* 2009; *20*, 455301.

[58] Cai J. Ruffieux P. Jaafar R. Bieri M. Braun T. Blankenburg S. Muoth M. Seitsonen A. P. Saleh M. Feng X. Mullen K. Fasel R. Atomically precise bottom-up fabrication of graphene nanoribbons, *Nature* 2010; *466*, 470–473.

[59] Barone V. Hod O. Scuseria G. E. Electronic Structure and Stability of Semiconducting Graphene Nanoribbons, *Nano Lett.* 2006; *6*, 2748–2754.

[60] Son Y.-W. Cohen M. L. Louie S. G. Energy Gaps in Graphene Nanoribbons, *Phys. Rev. Lett.* 2006; *97*, 216803.

[61] Yang L. Park C.-H. Son Y.-W. Cohen M. L. Louie S. G. Quasiparticle Energies and Band Gaps in Graphene Nanoribbons, *Phys. Rev. Lett.* 2007; *99*, 186801.

[62] Safron N. S. Brewer A. S. Arnold M. S. Semiconducting Two-Dimensional Graphene Nanoconstriction Arrays, *Small* 2011; *7*, 492–498.

[63] Sint K. Wang B. Král P. Selective Ion Passage through Functionalized Graphene Nanopores, *J. Am. Chem. Soc.* 2008; *130*, 16448–16449.

[64] Kim M. Safron N. S. Han E. Arnold M. S. Gopalan P. Fabrication and Characterization of Large-Area, Semiconducting Nanoperforated Graphene Materials, *Nano Lett.* 2010; *10*, 1125–1131.

[65] Wang X. Ouyang Y. Li X. Wang H. Guo J. Dai H. Room-Temperature All-Semiconducting Sub-10-nm Graphene Nanoribbon Field-Effect Transistors, *Phys. Rev. Lett.* 2008; *100*, 206803.

[66] Sun Z. James D. K. Tour J. M. Graphene Chemistry: Synthesis and Manipulation, *J. Phys. Chem. Lett.* 2011; *2*, 2425–2432.

[67] Pei H. Li J. Lv M. Wang J. Gao J. Lu J. Li Y. Huang Q. Hu J. Fan C. A Graphene-Based Sensor Array for High-Precision and Adaptive Target Identification with Ensemble Aptamers, *J. Am. Chem. Soc.* 2012; *134*, 13843–13849.

[68] Shen H. Zhang L. Liu M. Zhang Z. Biomedical Applications of Graphene, *Theranostics* 2012; *2(3)*, 283–294.

[69] Chen J.-H. Jang C. Xiao S. Ishigami M. Fuhrer M. S. Intrinsic and extrinsic performance limits of graphene devices on SiO2, *Nat Nano* 2008; *3*, 206–209.

[70] Schedin F. Geim A. K. Morozov S. V. Hill E. W. Blake P. Katsnelson M. I. Novoselov K. S. Detection of individual gas molecules adsorbed on graphene, *Nat Mater* 2007; *6*, 652–655.

[71] Jiang D.-e. Cooper V. R. Dai S. Porous Graphene as the Ultimate Membrane for Gas Separation, *Nano Lett.* 2009; *9*, 4019–4024.

[72] Suk M. E. Aluru N. R. Water Transport through Ultrathin Graphene, *J. Phys. Chem. Lett.* 2010; *1*, 1590–1594.

[73] Garaj S. Hubbard W. Reina A. Kong J. Branton D. Golovchenko J. A. Graphene as a subnanometre trans-electrode membrane, *Nature* 2010; *467*, 190–193.

[74] Sathe C. Zou X. Leburton J.-P. Schulten K. Computational Investigation of DNA Detection Using Graphene Nanopores, *ACS Nano* 2011; *5*, 8842–8851.

[75] Koenig S. P. Wang L. Pellegrino J. Bunch J. S. Selective molecular sieving through porous graphene, *Nat Nano* 2012; *7*, 728–732.

[76] Baskin A. Kral P. Electronic structures of porous nanocarbons, *Sci. Rep.* 2011; *1*, 36.

[77] Hauser A. W. Schwerdtfeger P. Nanoporous Graphene Membranes for Efficient 3He/4He Separation, *J. Phys. Chem. Lett.* 2011; *3*, 209–213.

[78] Hauser A. W. Schrier J. Schwerdtfeger P. Helium Tunneling through Nitrogen-Functionalized Graphene Pores: Pressure- and Temperature-Driven Approaches to Isotope Separation, *J. Phys. Chem. C* 2012; *116*, 10819–10827.

[79] Paul D. R. Creating New Types of Carbon-Based Membranes, *Science* 2012; *335*, 413–414.

[80] Nair R. R. Wu H. A. Jayaram P. N. Grigorieva I. V. Geim A. K. Unimpeded Permeation of Water Through Helium-Leak-ÂĂÂŞTight Graphene-Based Membranes, *Science* 2012; *335*, 442–444.

[81] Karan S. Samitsu S. Peng X. Kurashima K. Ichinose I. Ultrafast Viscous Permeation of Organic Solvents Through Diamond-Like Carbon Nanosheets, *Science* 2012; *335*, 444–447.

[82] Gong X. Li J. Xu K. Wang J. Yang H. A Controllable Molecular Sieve for Na+ and K+ Ions, *J. Am. Chem. Soc.* 2010; *132*, 1873–1877.

[83] Hankel M. Jiao Y. Du A. Gray S. K. Smith S. C. Asymmetrically Decorated, Doped Porous Graphene As an Effective Membrane for Hydrogen Isotope Separation, *J. Phys. Chem. C* 2012; *116*, 6672–6676.

[84] Venkatesan B. M. Estrada D. Banerjee S. Jin X. Dorgan V. E. Bae M.-H. Aluru N. R. Pop E. Bashir R. Stacked Graphene-Al2O3 Nanopore Sensors for Sensitive Detection of DNA and DNA-ÂĂÂŞProtein Complexes, *ACS Nano* 2011; *6*, 441–450.

[85] Fischbein M. D. Drndic M. Electron beam nanosculpting of suspended graphene sheets, *Appl. Phys. Lett.* 2008; *93*, 113107–3.

[86] Schneider G. F. Kowalczyk S. W. Calado V. E. Pandraud G. Zandbergen H. W. Vandersypen L. M. K. Dekker C. DNA Translocation through Graphene Nanopores, *Nano Lett.* 2010; *10*, 3163–3167.

[87] Merchant C. A. Healy K. Wanunu M. Ray V. Peterman N. Bartel J. Fischbein M. D. Venta K. Luo Z. Johnson A. T. C. DrndicÂĄ M. DNA Translocation through Graphene Nanopores, *Nano Lett.* 2010; *10*, 2915–2921.

[88] Fan Z. Zhao Q. Li T. Yan J. Ren Y. Feng J. Wei T. Easy synthesis of porous graphene nanosheets and their use in supercapacitors, *Carbon* 2012; *50*, 1699–1703.

[89] Han T. H. Huang Y.-K. Tan A. T. L. Dravid V. P. Huang J. Steam Etched Porous Graphene Oxide Network for Chemical Sensing, *J. Am. Chem. Soc.* 2011; *133*, 15264–15267.

[90] Bieri M. Treier M. Cai J. Ait-Mansour K. Ruffieux P. Groning O. Groning P. Kastler M. Rieger R. Feng X. Mullen K. Fasel R. Porous graphenes: two-dimensional polymer synthesis with atomic precision, *Chem. Commun.* 2009; , 6919–6921.

[91] Jia X. Campos-Delgado J. Terrones M. Meunier V. Dresselhaus M. S. Graphene edges: a review of their fabrication and characterization, *Nanoscale* 2011; *3*, 86–95.

[92] Luo Z. Yu T. Ni Z. Lim S. Hu H. Shang J. Liu L. Shen Z. Lin J. Electronic Structures and Structural Evolution of Hydrogenated Graphene Probed by Raman Spectroscopy, *J. Phys. Chem. C* 2011; *115*, 1422–1427.

[93] Mak K. F. Sfeir M. Y. Misewich J. A. Heinz T. F. The evolution of electronic structure in few-layer graphene revealed by optical spectroscopy, *Proc. Natl. Acad. Sci USA* 2010; *107*, 14999–15004.

[94] Li Z. Q. Henriksen E. A. Jiang Z. Hao Z. Martin M. C. Kim P. Stormer H. L. Basov D. N. Band Structure Asymmetry of Bilayer Graphene Revealed by Infrared Spectroscopy, *Phys. Rev. Lett.* 2009; *102*, 037403.

[95] Zhang L. M. Li Z. Q. Basov D. N. Fogler M. M. Hao Z. Martin M. C. Determination of the electronic structure of bilayer graphene from infrared spectroscopy, *Phys. Rev. B* 2008; *78*, 235408.

[96] Phark S.-h. Borme J. Vanegas A. L. Corbetta M. Sander D. Kirschner J. Atomic structure and spectroscopy of graphene edges on Ir(111), *Phys. Rev. B* 2012; *86*, 045442.

[97] Yang X. X. Li J. W. Zhou Z. F. Wang Y. Yang L. W. Zheng W. T. Sun C. Q. Raman spectroscopic determination of the length, strength, compressibility, Debye temperature, elasticity, and force constant of the C-C bond in graphene, *Nanoscale* 2012; *4*, 502–510.

[98] Li Z. Lui C. H. Cappelluti E. Benfatto L. Mak K. F. Carr G. L. Shan J. Heinz T. F. Structure-Dependent Fano Resonances in the Infrared Spectra of Phonons in Few-Layer Graphene, *Phys. Rev. Lett.* 2012; *108*, 156801.

[99] Kudin K. N. Ozbas B. Schniepp H. C. Prud'homme R. K. Aksay I. A. Car R. Raman Spectra of Graphite Oxide and Functionalized Graphene Sheets, *Nano Lett.* 2007; *8*, 36–41.

[100] Niyogi S. Bekyarova E. Itkis M. E. Zhang H. Shepperd K. Hicks J. Sprinkle M. Berger C. Lau C. N. deHeer W. A. Conrad E. H. Haddon R. C. Spectroscopy of Covalently Functionalized Graphene, *Nano Lett.* 2010; *10*, 4061–4066.

[101] Daniels K. M. Daas B. K. Srivastava N. Williams C. Feenstra R. M. Sudarshan T. S. Chandrashekhar M. V. S. Evidences of electrochemical graphene functionalization and substrate dependence by Raman and scanning tunneling spectroscopies, *J. Appl. Phys.* 2012; *111*, 114306–7.

[102] Graf D. Molitor F. Ensslin K. Stampfer C. Jungen A. Hierold C. Wirtz L. Spatially Resolved Raman Spectroscopy of Single- and Few-Layer Graphene, *Nano Lett.* 2007; *7*, 238–242.

[103] Ferrari A. C. Meyer J. C. Scardaci V. Casiraghi C. Lazzeri M. Mauri F. Piscanec S. Jiang D. Novoselov K. S. Roth S. Geim A. K. Raman Spectrum of Graphene and Graphene Layers, *Phys. Rev. Lett.* 2006; *97*, 187401.

[104] Calizo I. Balandin A. A. Bao W. Miao F. Lau C. N. Temperature Dependence of the Raman Spectra of Graphene and Graphene Multilayers, *Nano Lett.* 2007; *7*, 2645–2649.

[105] Malard L. Pimenta M. Dresselhaus G. Dresselhaus M. Raman spectroscopy in graphene, *Physics Reports* 2009; *473*, 51–87.

[106] Schedin F. Lidorikis E. Lombardo A. Kravets V. G. Geim A. K. Grigorenko A. N. Novoselov K. S. Ferrari A. C. Surface-Enhanced Raman Spectroscopy of Graphene, *ACS Nano* 2010; *4*, 5617–5626.

[107] Li Z. Q. Henriksen E. A. Jiang Z. Hao Z. Martin M. C. Kim P. Stormer H. L. Basov D. N. Dirac charge dynamics in graphene by infrared spectroscopy, *Nat Phys* 2008; *4*, 532–535.

[108] Mak K. F. Lui C. H. Shan J. Heinz T. F. Observation of an Electric-Field-Induced Band Gap in Bilayer Graphene by Infrared Spectroscopy, *Phys. Rev. Lett.* 2009; *102*, 256405.

[109] Jiang Z. Henriksen E. A. Tung L. C. Wang Y.-J. Schwartz M. E. Han M. Y. Kim P. Stormer H. L. Infrared Spectroscopy of Landau Levels of Graphene, *Phys. Rev. Lett.* 2007; *98*, 197403.

[110] Eberlein T. Bangert U. Nair R. R. Jones R. Gass M. Bleloch A. L. Novoselov K. S. Geim A. Briddon P. R. Plasmon spectroscopy of free-standing graphene films, *Phys. Rev. B* 2008; *77*, 233406.

[111] Dora B. Simon F. Unusual Hyperfine Interaction of Dirac Electrons and NMR Spectroscopy in Graphene, *Phys. Rev. Lett.* 2009; *102*, 197602.

[112] Li G. Luican A. Andrei E. Y. Scanning Tunneling Spectroscopy of Graphene on Graphite, *Phys. Rev. Lett.* 2009; *102*, 176804.

[113] Ohta T. Bostwick A. McChesney J. L. Seyller T. Horn K. Rotenberg E. Interlayer Interaction and Electronic Screening in Multilayer Graphene Investigated with Angle-Resolved Photoemission Spectroscopy, *Phys. Rev. Lett.* 2007; *98*, 206802.

[114] Xu M. Fujita D. Gao J. Hanagata N. Auger Electron Spectroscopy: A Rational Method for Determining Thickness of Graphene Films, *ACS Nano* 2010; *4*, 2937–2945.

[115] Ackerman M. Clapham D. Mechanisms of disease - Ion channels - Basic science and clinical disease, *N Engl J Med* 1997; *336*, 1575–1586.

[116] Yu J. Yool A. J. Schulten K. Tajkhorshid E. Mechanism of gating and ion conductivity of a possible tetrameric pore in aquaporin-1, *Structure* 2006; *14*, 1411–1423.

[117] Jordan E. Bell R. G. Wilmer D. Koller H. Anion-Promoted Cation Motion and Conduction in Zeolites, *J. Am. Chem. Soc.* 2005; *128*, 558–567.

[118] Saufi S. Ismail A. Fabrication of carbon membranes for gas separation, *Carbon* 2004; *42*, 241–259.

[119] Duke M. C. Costa da J. C. D. Do D. D. Gray P. G. Lu G. Q. Hydrothermally Robust Molecular Sieve Silica for Wet Gas Separation, *Adv.Funct. Mater.* 2006; *16*, 1215–1220.

[120] Ghadiri M. R. Granja J. R. Buehler L. K. Artificial transmembrane ion channels from self-assembling peptide nanotubes, *Nature* 1994; *369*, 301–304.

[121] Kobuke Y. Ueda K. Sokabe M. Artificial non-peptide single ion channels, *J. Am. Chem. Soc.* 1992; *114*, 7618–7622.

[122] Hummer G. Rasaiah J. C. Noworyta J. P. Water conduction through the hydrophobic channel of a carbon nanotube, *Nature* 2001; *414*, 188–190.

[123] Skoulidas A. I. Ackerman D. M. Johnson J. K. Sholl D. S. Rapid Transport of Gases in Carbon Nanotubes, *Phys. Rev. Lett.* 2002; *89*, 185901.

[124] Holt J. K. Park H. G. Wang Y. Stadermann M. Artyukhin A. B. Grigoropoulos C. P. Noy A. Bakajin O. Fast Mass Transport Through Sub-2-Nanometer Carbon Nanotubes, *Science* 2006; *312*, 1034–1037.

[125] Majumder M. Chopra N. Andrews R. Hinds B. J. Nanoscale hydrodynamics: Enhanced flow in carbon nanotubes, *Nature* 2005; *438*, 44–44.

[126] Wang Z. Ci L. Chen L. Nayak S. Ajayan P. M. Koratkar N. Polarity-Dependent Electrochemically Controlled Transport of Water through Carbon Nanotube Membranes, *Nano Lett.* 2007; *7*, 697–702.

[127] Zhou J. Noca F. Gharib M. Flow conveying and diagnosis with carbon nanotube arrays, *Nanotechnology* 2006; *17*, 4845âĂŞ4853.

[128] Whitby M. Quirke N. Fluid flow in carbon nanotubes and nanopipes, *Nat Nano* 2007; *2*, 87–94.

[129] Liu H. Murad S. C.J. J. Ion permeation dynamics in carbon nanotubes, *J. Chem. Phys.* 2006; *125*, 084713.

[130] Corso M. Auwörter W. Muntwiler M. Tamai A. Greber T. Osterwalder J. Boron Nitride Nanomesh, *Science* 2004; *303*, 217–220.

[131] Geim A. K. Novoselov K. S. The rise of graphene, *Nat Mater* 2007; *6*, 183–191.

[132] Berner S. Corso M. Widmer R. Groening O. Laskowski R. Blaha P. Schwarz K. Goriachko A. Over H. Gsell S. Schreck M. Sachdev H. Greber T. Osterwalder J. Boron Nitride Nanomesh: Functionality from a Corrugated Monolayer, *Angew. Chem. Int. Ed.* 2007; *46*, 5115–5119.

[133] Laskowski R. Blaha P. Gallauner T. Schwarz K. Single-Layer Model of the Hexagonal Boron Nitride Nanomesh on the Rh(111) Surface, *Phys. Rev. Lett.* 2007; *98*, 106802.

[134] Ohta T. Bostwick A. Seyller T. Horn K. Rotenberg E. Controlling the Electronic Structure of Bilayer Graphene, *Science* 2006; *313*, 951–954.

[135] Bunch J. S. Verbridge S. S. Alden J. S. Zande van der A. M. Parpia J. M. Craighead H. G. McEuen P. L. Impermeable Atomic Membranes from Graphene Sheets, *Nano Lett.* 2008; *8*, 2458–2462.

[136] Liu Y. Dong X. Chen P. Biological and chemical sensors based on graphene materials, *Chem. Soc. Rev.* 2012; *41*, 2283–2307.

[137] Jagerszki G. Takacs A. Bitter I. Gyurcsanyi R. E. Solid-State Ion Channels for Potentiometric Sensing, *Angew. Chem. Int. Ed.* 2011; *50*, 1656–1659.

[138] Titov A. V. Wang B. Sint K. Král P. Controllable Synthetic Molecular Channels: Biomimetic Ammonia Switch, *J. Phys. Chem. B* 2009; *114*, 1174–1179.

[139] Stampfer C. Guttinger J. Molitor F. Graf D. Ihn T. Ensslin K. Tunable Coulomb blockade in nanostructured graphene, *Appl. Phys. Lett.* 2008; *92*, 012102–3.

[140] Stankovich S. Dikin D. A. Dommett G. H. B. Kohlhaas K. M. Zimney E. J. Stach E. A. Piner R. D. Nguyen S. T. Ruoff R. S. Graphene-based composite materials, *Nature* 2006; *442*, 282–286.

[141] Gilje S. Han S. Wang M. Wang K. L. Kaner R. B. A Chemical Route to Graphene for Device Applications, *Nano Lett.* 2007; *7*, 3394–3398.

[142] The NVT ensemble with periodic boundary conditions is used, where the electrostatic coupling is calculated by the PME method. The Langevin dynamics is applied to the systems with the damping coefficient of 0.01 ps-1, in order to minimize the unphysical loss of momenta to the reservoirs. The time step is always 1 fs.

[143] Darden T. York D. Pedersen L. Particle Mesh Ewald-an N.Log(N) method for Ewald sums in large systems, *J. Chem. Phys.* 1993; *98*, 10089–10092.

[144] Wang B. Král P. Coulombic Dragging of Molecules on Surfaces Induced by Separately Flowing Liquids, *J. Am. Chem. Soc.* 2006; *128*, 15984–15985.

[145] Phillips J. Braun R. Wang W. Gumbart J. Tajkhorshid E. Villa E. Chipot C. Skeel R. Kale L. K. S. Scalable molecular dynamics with NAMD, *J. Comput. Chem.* 2005; *26*, 1781–1802.

[146] MacKerell A. D. Bashford D. Bellott Dunbrack R. L. Evanseck J. D. Field M. J. Fischer S. Gao J. Guo H. Ha S. Joseph-McCarthy D. Kuchnir L. Kuczera K. Lau F. T. K. Mattos C. Michnick S. Ngo T. Nguyen D. T. Prodhom B. Reiher W. E. Roux B. Schlenkrich M. Smith J. C. Stote R. Straub J. Watanabe M. Wiórkiewicz-Kuczera J. Yin D. Karplus M. All-Atom Empirical Potential for Molecular Modeling and Dynamics Studies of Proteins, *J. Phys. Chem. B* 1998; *102*, 3586–3616.

[147] The calculations are done with 3-21g basis set. Charges are obtained by the Natural Population analysis.

[148] Frisch M. et al. *Gaussian 03, Revision C.02* 2004; *Gaussian, Inc., Wallingford, C.T.*

[149] Auffinger P. Bielecki L. Westhof E. Symmetric K^+ and Mg^{2+} ion-binding sites in the 5S rRNA loop E inferred from molecular dynamics simulations, *J. Mol. Biol.* 2004; *335(2)*, 555–571.

[150] Wang B. Král P. Cover Picture: Optimal Atomistic Modifications of Material Surfaces: Design of Selective Nesting Sites for Biomolecules (Small 4/2007), *Small* 2007; *3*, 580–584.

[151] Merlet C. Rotenberg B. Madden P. A. Taberna P.-L. Simon P. Gogotsi Y. Salanne M. On the molecular origin of supercapacitance in nanoporous caaarbon electrodes, *Nat Mater* 2012; *11*, 306–310.

[152] Du H. Li J. Zhang J. Su G. Li X. Zhao Y. Separation of Hydrogen and Nitrogen Gases with Porous Graphene Membrane, *J. Phys. Chem. C* 2011; *115*, 23261–23266.

[153] Shan M. Xue Q. Jing N. Ling C. Zhang T. Yan Z. Zheng J. Influence of chemical functionalization on the CO_2/N_2 separation performance of porous graphene membranes, *Nanoscale* 2012; *4*, 5477–5482.

[154] Hauser A. W. Schwerdtfeger P. Methane-selective nanoporous graphene membranes for gas purification, *Phys. Chem. Chem. Phys.* 2012; *14*, 13292–13298.

[155] Blankenburg S. Bieri M. Fasel R. Müllen K. Pignedoli C. A. Passerone D. Porous Graphene as an Atmospheric Nanofilter, *Small* 2010; *6*, 2266–2271.

[156] Wang E. N. Karnik R. Water desalination: Graphene cleans up water, *Nat Nano* 2012; *7*, 552–554.

[157] Cohen-Tanugi D. Grossman J. C. Water Desalination across Nanoporous Graphene, *Nano Lett.* 2012; *12*, 3602–3608.

[158] Bae S. Kim H. Lee Y. Xu X. Park J.-S. Zheng Y. Balakrishnan J. Lei T. Ri Kim H. Song Y. I. Kim Y.-J. Kim K. S. Ozyilmaz B. Ahn J.-H. Hong B. H. Iijima S. Roll-to-roll production of 30-inch graphene films for transparent electrodes, *Nat Nano* 2010; *5*, 574–578.

[159] Venkatesan B. M. Bashir R. Nanopore sensors for nucleic acid analysis, *Nat Nano* 2011; *6*, 615–624.

[160] Wells D. B. Belkin M. Comer J. Aksimentiev A. Assessing Graphene Nanopores for Sequencing DNA, *Nano Lett.* 2012; *12*, 4117–4123.

[161] Postma H. W. C. Rapid Sequencing of Individual DNA Molecules in Graphene Nanogaps, *Nano Lett.* 2010; *10*, 420–425.

[162] Nelson T. Zhang B. Prezhdo O. V. Detection of Nucleic Acids with Graphene Nanopores: Ab Initio Characterization of a Novel Sequencing Device, *Nano Lett.* 2010; *10*, 3237–3242.

[163] Saha K. K. Drndic M. Nikolic B. K. DNA Base-Specific Modulation of Microampere Transverse Edge Currents through a Metallic Graphene Nanoribbon with a Nanopore, *Nano Lett.* 2011; *12*, 50–55.

[164] Palacios J. J. Fernández-Rossier J. Brey L. Vacancy-induced magnetism in graphene and graphene ribbons, *Phys. Rev. B* 2008; *77*, 195428.

[165] Balog R. Jorgensen B. Nilsson L. Andersen M. Rienks E. Bianchi M. Fanetti M. Laegsgaard E. Baraldi A. Lizzit S. Sljivancanin Z. Besenbacher F. Hammer B. Pedersen T. G. Hofmann P. Hornekaer L. Bandgap opening in graphene induced by patterned hydrogen adsorption, *Nat Mater* 2010; *9*, 315–319.

[166] Cervantes-Sodi F. Csányi G. Piscanec S. Ferrari A. C. Edge-functionalized and substitutionally doped graphene nanoribbons: Electronic and spin properties, *Phys. Rev. B* 2008; *77*, 165427.

[167] Furst J. A. Pedersen J. G. Flindt C. Mortensen N. A. Brandbyge M. Pedersen T. G. Jauho A.-P. Electronic properties of graphene antidot lattices, *New Journal of Physics* 2009; *11*, 095020.

[168] Pedersen T. G. Flindt C. Pedersen J. Mortensen N. A. Jauho A.-P. Pedersen K. Graphene Antidot Lattices: Designed Defects and Spin Qubits, *Phys. Rev. Lett.* 2008; *100*, 136804.

[169] Vanevic M. Stojanovic V. M. Kindermann M. Character of electronic states in graphene antidot lattices: Flat bands and spatial localization, *Phys. Rev. B* 2009; *80*, 045410.

[170] Gao Y.-D. Kumazaki H. Terai J. Chida K. Hosoya H. Topological factors governing the HOMO-LUMO band gap of the density of states of periodic hydrocarbon polymer networks, *Journal of Mathematical Chemistry* 1993; *12*, 279–308.

[171] Fujita M. Wakabayashi K. Nakada K. Kusakabe K. Peculiar localized states at zigzag graphite edges, *J. Phys. Soc. Jpn.* 1996; *65*, 1920.

[172] Shima N. Aoki H. Electronic structure of super-honeycomb systems: A peculiar realization of semimetal/semiconductor classes and ferromagnetism, *Phys. Rev. Lett.* 1993; *71*, 4389–4392.

[173] Sato T. Imade M. Yamabe T. Electronic structure of porous nanotube, *Synthetic Metals* 1999; *103*, 2519–2520.

[174] Hatanaka M. Band structures of porous graphehes, *Chem. Phys. Lett.* 2010; *488*, 187.

[175] Ivanciuc O. Bytautas L. Klein D. J. Mean-field resonating-valencebond theory for unpaired π-electrons in benzenoid carbon species, *J. Chem. Phys.* 2002; *116*, 4735.

[176] Nakada K. Fujita M. Dresselhaus G. Dresselhaus M. S. Edge state in graphene ribbons: Nanometer size effect and edge shape dependence, *Phys. Rev. B* 1996; *54*, 17954–17961.

[177] Miyamoto Y. Nakada K. Fujita M. First-principles study of edge states of H-terminated graphitic ribbons, *Phys. Rev. B* 1999; *59*, 9858–9861.

[178] Ezawa M. Peculiar width dependence of the electronic properties of carbon nanoribbons, *Phys. Rev. B* 2006; *73*, 045432.

[179] Pisani L. Chan J. A. Montanari B. Harrison N. M. Electronic structure and magnetic properties of graphitic ribbons, *Phys. Rev. B* 2007; *75*, 064418.

[180] Yu S. Wen Q. Zheng W. Jiang Q. Electronic properties of graphene nanoribbons with armchair-shaped edges, *Molecular Simulation* 2008; *34*, 1085–1090.

[181] Kharche N. Zhou Y. O'ÂĂÂŹBrien K. P. Kar S. Nayak S. K. Effect of Layer Stacking on the Electronic Structure of Graphene Nanoribbons, *ACS Nano* 2011; *5*, 6096–6101.

[182] Sanchez-Portal D. Ordejon P. Artacho E. Soler J. M. Density-functional method for very large systems with LCAO basis sets, *Int. J. Quantum Chem.* 1997; *65*, 453–461.

[183] Perdew J. P. Zunger A. Self-interaction correction to density-functional approximations for many-electron systems, *Phys. Rev. B* 1981; *23*, 5048–5079.

[184] Lu Y. H. et al. Effects of edge passivation by hydrogen on electronic structure of armchair graphene nanoribbons and band gap engineering, *Appl. Phys. Lett.* 2009; *94*, 122111.

[185] Boukhvalov D. W. Katsnelson M. I. Lichtenstein A. I. Hydrogen on graphene: Electronic structure, total energy, structural distortions and magnetism from first-principles calculations, *Phys. Rev. B* 2008; *77*, 035427.

[186] Weiss D. Roukes M. L. Menschig A. Grambow P. Klitzing von K. Weimann G. Electron pinball and commensurate orbits in a periodic array of scatterers, *Phys. Rev. Lett.* 1991; *66*, 2790–2793.

[187] Flindt C. Mortensen N. A. Jauho A.-P. Quantum Computing via Defect States in Two-Dimensional Antidot Lattices, *Nano Lett.* 2005; *5*, 2515–2518.

[188] Pedersen J. Flindt C. Asger Mortensen N. Jauho A.-P. Spin qubits in antidot lattices, *Phys. Rev. B* 2008; *77*, 045325–.

[189] Lieb E. H. Two theorems on the Hubbard model, *Phys. Rev. Lett.* 1989; *62*, 1201–1204.

[190] Inui M. Trugman S. A. Abrahams E. Unusual properties of midband states in systems with off-diagonal disorder, *Phys. Rev. B* 1994; *49*, 3190–3196.

[191] Fazekas P., *Lecture Notes on Electron Correlation and Magnetism* (World Scientific, New York, 1999).

[192] Tylianakis E. Dimitrakakis G. K. Melchor S. Dobado J. A. Froudakis G. E. Porous nanotube network: a novel 3-D nanostructured material with enhanced hydrogen storage capacity, *Chem. Commun.* 2011; *47*, 2303–2305.

[193] Zhang J. Ong K. P. Wu P. The Influence of Out-of-Plane Deformation on the Band Gap of Graphene Nanoribbons, *J. Phys. Chem. C* 2010; *114*, 12749–12753.

[194] Lu Y. Guo J. Band gap of strained graphene nanoribbons, *Nano Research* 2010; *3*, 189–199.

[195] Banhart F. Kotakoski J. Krasheninnikov A. V. Structural Defects in Graphene, *ACS Nano* 2010; *5*, 26–41.

[196] Mele E. J. Král P. Electric Polarization of Heteropolar Nanotubes as a Geometric Phase, *Phys. Rev. Lett.* 2002; *88*, 056803.

[197] Xue Y. Ratner M. A. Microscopic study of electrical transport through individual molecules with metallic contacts. I. Band lineup, voltage drop, and high-field transport, *Phys. Rev. B* 2003; *68*, 115406.

[198] Bauschlicher J., Charles W. Lawson J. W. Current-voltage curves for molecular junctions: Effect of substitutients, *Phys. Rev. B* 2007; *75*, 115406.

[199] Sahin H. Senger R. T. First-principles calculations of spin-dependent conductance of graphene flakes, *Phys. Rev. B* 2008; *78*, 205423.

[200] Dubois S. M.-M. Zanolli Z. Declerck X. Charlier J.-C. Electronic properties and quantum transport in Graphene-based nanostructures, *Eur. Phys. J. B* 2009; *72*, 1–24.

[201] Topsakal M. Bagci V. M. K. Ciraci S. Current-voltage (I-V) characteristics of armchair graphene nanoribbons under uniaxial strain, *Phys. Rev. B* 2010; *81*, 205437.

[202] Terrones M. Botello-Mendez A. R. Campos-Delgado J. Lopez-Urias F. Vega-Cantu Y. I. Rodriguez-Macias F. J. Elias A. L. Munoz-Sandoval E. Cano-Márquez A. G. Charlier J.-C. Terrones H. Graphene and graphite nanoribbons: Morphology, properties, synthesis, defects and applications, *Nano Today* 2010; *5*, 351–372.

[203] Kim W. Y. Kim K. S. Prediction of very large values of magnetoresistance in a graphene nanoribbon device, *Nat Nano* 2008; *3*, 408–412.

[204] Biel B. Blase X. Triozon F. Roche S. Anomalous Doping Effects on Charge Transport in Graphene Nanoribbons, *Phys. Rev. Lett.* 2009; *102*, 096803.

[205] Datta S. *Electronic Transport in Mesoscopic Systems* (Cambridge University Press, Cambridge, England, 1995).

[206] Brandbyge M. Mozos J.-L. Ordejón P. Taylor J. Stokbro K. Density-functional method for nonequilibrium electron transport, *Phys. Rev. B* 2002; *65*, 165401.

[207] Hansen T. Solomon G. C. Andrews D. Q. Ratner M. A. Interfering pathways in benzene: An analytical treatment, *J. Chem. Phys.* 2009; *131*, 194704–12.